Physicochemical Study on Biological Membrane Penetration of Arginine-rich peptides

2015

Yuki Haraya

Contents

Abbreviations

ATR-FTIR: attenuated total reflection-Fourier transform infrared

BBM: biotechnology-based medicine

CD: circular dichroism

CLSM: confocal laser scanning microscopy

CPPs: cell penetrating peptides

Dansyl-PE: 1,2-dioleoyl-*sn*-glycero-3-phosphoethanolamine-*N*-(5-dimethylamino-1-naphthalenesulfonyl)

DPH: 1,6-diphenyl-1,3,5-hexatriene

EPC: egg phosphatidylcholine

EPG: egg phosphatidylglycerol

FAM: 5(6)-carboxyfluorescein

GAG: glycosaminoglycan

HL60: human myeloid leukemia cells

ITC: isothermal titration calorimetry

LUV: large unilamellar vesicle

PLA: poly-L-arginine

PLL: poly-L-lysine

R8: octaarginine

SBPL: soybean phospholipid

TFE: 2,2,2-trifluoroethanol

TMA-DPH: *N*,*N*,*N*-trimethyl-4-(6-phenyl-1,3,5-hexatrien-1-yl)phenylammonium

WMF: wavelength of maximum fluorescence

1. INTRODUCTION

As biotechnologies such as proteomics and genomics give an ever greater understanding of disease at molecular level, the number of biotechnology-based molecules (BBMs) including oligonucleotide, plasmids, peptides, and proteins is increasing. In contrast, the rate of drug discovery based on classical, small-molecule drugs is decreasing. The reason comes from the need to target protein-protein interactions, reach targets intra-cellular site and achieve specificity for effective medical treatment of diseases.[1] Therefore, pharmaceutical companies tend to develop approaches that enable a rapid rational design of active and specific BBM. Antibodies, peptide mimetics, and siRNAs are prominent examples. However, for these molecules, success rates in drug discovery are very low. It is estimated that 90 % of fund for research and development in BBMs go to waste.[1] One of the underlying reasons is the presence of the hydrophobic nature of the cell membrane that protects cells from influx of exogenous BBMs. One of the most potent strategies to deliver such poorly membrane-permeating BBMs into cells is to use cell-penetrating peptides (CPPs) rich in arginine residues, e.g. penetratin, pVEC, Tat-peptide, and polyarginine.[2,3] Although CPPs are considered to be promising drug delivery tools due to their ability to carry various BBMs across cell membranes *in vitro* and *in vivo*,[4,5] the cell entry mechanism of CPPs is still not fully understood.[6]

Two types of mechanisms in CPP's cell entry are being considered: one is endocytic pathway and another is energy-independent, non-endocytic pathway, that is, physical membrane penetration (Fig. 1).[7,8] For the endocytosis uptake of CPPs, more than 90 % of the delivered cargoes become biologically inactive due to being trapped in endosome compartments.[9] In contrast, the latter process circumvents the lysosomal degradation of cargo molecules with CPP. The first step in the membrane penetration of CPPs is their binding to the membrane phospholipids and/or proteoglycans such as heparan sulfate at the cell surface.[10–14] Thus, to design the peptide sequences which have a more rational cell penetration pathway, the knowledge from physicochemical view about the interactions

of CPPs with lipid membranes and proteoglycans is of fundamental importance.

In this thesis, physicochemical studies are conducted to investigate the mechanism for non-endocytotic direct membrane penetration of arginine-rich peptides.

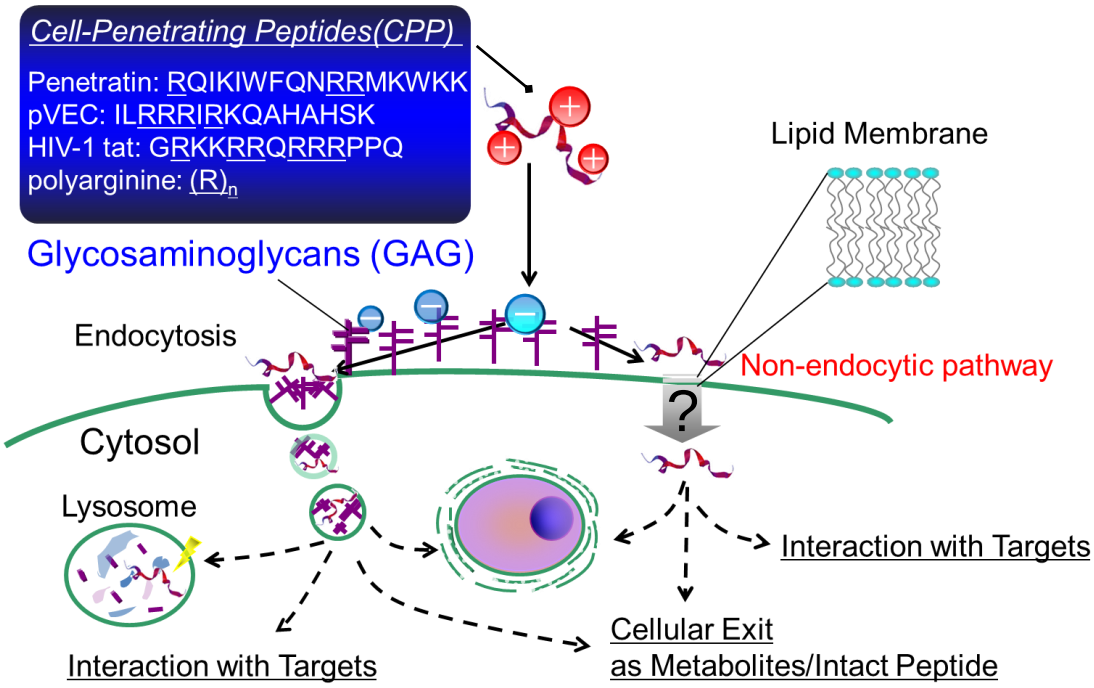

Fig.1. Cellular uptake of cell-penetrating peptides.

2. PHYSICOCHEMICAL MECHANISM FOR THE ENHANCED ABILITY OF LIPID MEMBRANE PENETRATION OF POLYARGININE

2.1. Introduction

The roles of arginine residue in CPP sequences have been studied in detail.[15–17] Arginine polymers enter cells more efficiently compared to lysine polymers with similar chain length.[18] Also, it was reported that the penetratin analogue in which arginine residues were substituted for lysines exhibited no cellular uptake at all.[19] These results suggest that guanidine moiety attached to the side chain of arginine is a key structure in the membrane permeation of peptides. In this regard, the ability of the guanidino group to form strong bidentate hydrogen bonds with phosphate group of phospholipid molecule seems to play a role for the membrane penetration.[20,21] In fact, conjugates of poly- and oligoarginines with amphiphilic anions, such as aliphatic acids, sulphates, or phosphates, are preferred to distribute into hydrophobic solvents such as octanol and chloroform.[22–24] Due to its ability to adapt to different environments by anion binding, polyarginine is titled as "molecular chameleon". [25]

Despite of the large interest in such "arginine magic",[23,26] only a few articles are available dealing with defined model systems to elucidate the detailed translocation mechanism of arginine polymers into lipid membranes. There are some reports about the polyarginine-membrane interaction but they only focused on the binding mechanism as the first step for the membrane penetration.[27–29] Because it is reported that none of CPPs are able to translocate across the membranes of large unilamellar vesicle (LUV) whereas they rapidly traverse the giant vesicles,[30,31] it seems that a choice of the model system is crucial for evaluation of the ability of polyarginine to penetrate lipid

membranes.

In this chapter, we examined the effects of chain length of polyarginine on its interaction with LUV or giant vesicle composed of anionic soybean phospholipids (SBPL) using poly-L-arginine composed of 69 (PLA69), 293 (PLA293), or 554 (PLA554) arginine residues, together with octaarginine (R8). To answer the question of how arginine and lysisne residues play a role on interactions of CPPs with cell membranes, interaction of PLA293 or poly-L-lysine (PLL) composed of 266 lysine residues with SBPL membrane was also examined.

2.2. Secondary structure of polyarginine in solution or bound to lipid membrane

It is known that lipid membranes have a dielectric constant, ε_r, gradient of which ~70 at the membrane surface, 30–40 at the membrane interface,[32] and ~5 at the hydrocarbon center.[33,34] To examine the effect of the dielectric constant on the secondary structure of polyarginine, we measured Circular Dichroism (CD) spectra of polyarginine in aqueous buffer/ethanol solutions with different polarities. ε_r of mixed solutions was calculated from the following equation:

$$\varepsilon_r = 78.3V_{water} + 25.37V_{ethanol} \quad \text{(Eq. 1)}$$

where 78.3 and 25.37 are ε_r of water and ethanol at 25 °C, respectively, V_{water} and $V_{ethanol}$ are volume fraction of aqueous buffer and ethanol, respectively. Fig. 2A shows CD spectra of PLA554 in Tris buffer/ethanol mixtures with different polarities. In Tris buffer (ε_r = 78), PLA554 exhibited a typical random coil structure (negative peak at ~190 nm and positive peak at ~215 nm). With decreasing the dielectric constant, the secondary structure of PLA554 changed from random coil to α-helix (negative peaks at ~208 and ~222 nm, positive peak at ~190 nm). Fig. 2B compares the change in secondary structure of polyarginines at different dielectric constant environment. This indicates that the degree of transition from random coil to α-helix in the low ε_r environment is much greater for the

longer polyarginine, especially PLA554.

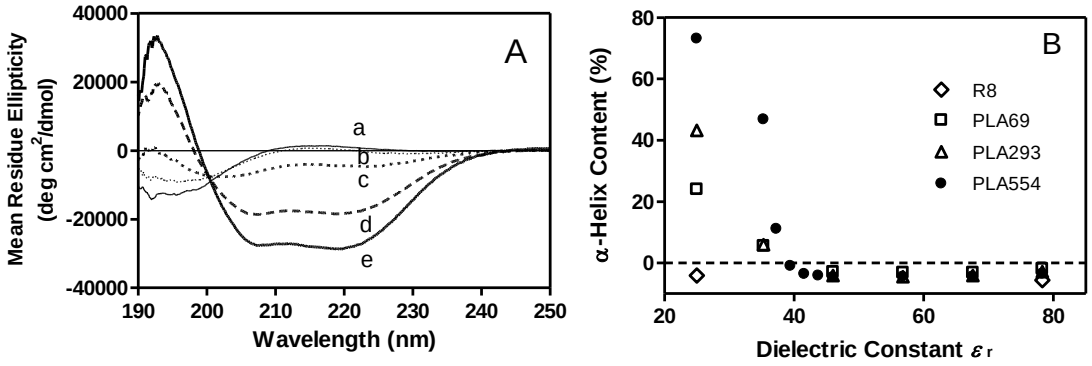

Fig. 2. (A) Far-UV CD spectra of PLA554 in aqueous buffer/ethanol mixtures. The volume fraction of ethanol was (a) 0, (b) 72, (c) 76, (d) 80 and (e) 99%, corresponding to the dielectric constant of 78, 39, 37, 35 and 25, respectively. The concentration of polyarginine was 0.3 residual mM. (B) α-Helix contents of polyarginine calculated from $[\theta]_{222}$ were plotted as a function of the dielectric constant of solvent. Reproduced in part with permission from *Langmuir* 2011, **27**, 7101. © 2011 American Chemical Society.

We next examined the structural change of polyarginine upon binding to LUV. Fig. 3 shows CD spectra of polyarginine in the presence of SBPL LUV, demonstrating that the lipid binding induced a slight, but significant change in secondary structure from random coil to α-helix for PLA293 and PLA554, whereas R8 and PLA69 still exhibited random coil or random coil-like structure. The calculated α-helix content (4.3 and 10.8% for PLA293 and PLA554, respectively) corresponds to 13 and 60 arginines in the α-helical structure for PLA293 and PLA554, respectively. Interestingly, from these α-helix contents of PLA293 and PLA554, the dielectric constant environment for PLA bound to LUV is estimated to be about 35–37 based on the dielectric analysis shown in Fig. 2B. This suggests that PLA is bound at the membrane interface region.

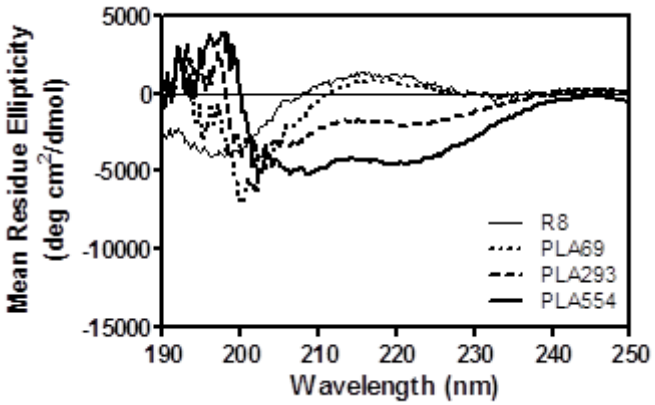

Fig. 3. Far-UV CD spectra of polyarginines bound to SBPL LUV. The phospholipid concentration was 0.5 mM. The concentrations of PLA and R8 were 0.1 and 0.4 residual mM, respectively. Reproduced in part with permission from *Langmuir* 2011, **27**, 7101. © 2011 American Chemical Society.

2.3. Effects of binding of polyarginine on structure of lipid membrane

To investigate the effects of binding of polyarginine on the structure of the hydrocarbon region in SBPL membranes, we measured fluorescence anisotropy of membrane probes, 1,6-diphenyl-1,3,5-hexatriene (DPH) and *N*,*N*,*N*-trimethyl-4-(6-phenyl-1,3,5-hexatrien-1-yl)phenyl-ammonium (TMA-DPH) embedded in LUV. Because DPH and TMA-DPH are located around 7.8 and 10.9 Å from the hydrophobic center of lipid bilayer, respectively, the fluorescence anisotropy of these probes reflects the fluidity of the hydrocarbon region in membrane.[35,36] As shown in Fig. 4A, the finding that the fluorescence anisotropy value, *r*, of DPH and TMA-DPH in LUV was not affected by binding of polyarginine indicates that there is no detectable interaction between polyarginine and the hydrocarbon region of SBPL membranes in the equilibrium state.

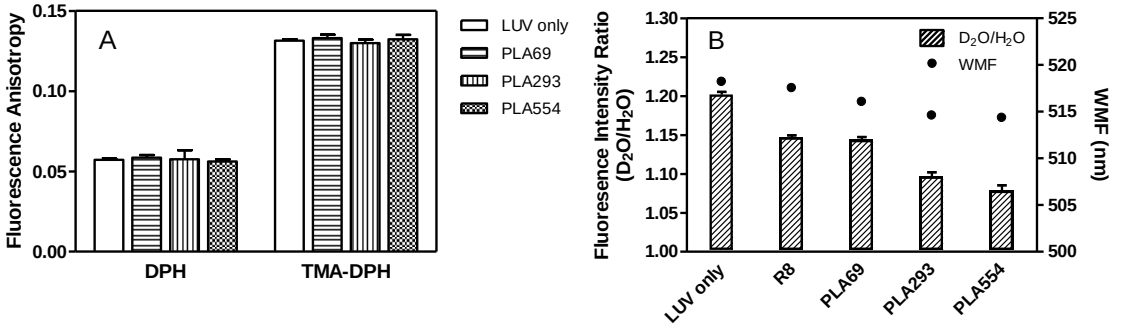

Fig. 4. (A) Effects of PLA binding on fluorescence anisotropy of DPH and TMA-DPH in SBPL LUV. (B) Effects of polyarginine binding on D_2O/H_2O fluorescence intensity ratio and wavelength of maximum fluorescence of dansyl-PE in SBPL LUV. Phospholipid concentration was 0.1 mM and the concentrations of PLA and R8 were 0.1 and 0.003 residual mM, respectively. Reproduced in part with permission from *Langmuir* 2011, **27**, 7102. © 2011 American Chemical Society.

We next used dansyl-PE as a membrane probe for the interface region as its dansyl group is located around 19 Å from the bilayer center.[37] The wavelength of maximum fluorescence (WMF) and deuterium isotope exchange of dansyl-PE were used to assess the degree of hydration and packing in the interface region of LUV. The dansyl fluorophor with an exchangeable hydrogen such as dansyl-PE is known to have a greater quantum yield in D_2O relative to H_2O due to a reduced rate of proton transfer. An increase in fluorescence intensity of dansyl-PE in D_2O compared to that in H_2O, therefore, indicates exposure of the probe to water, and the D_2O/H_2O intensity ratio reflects the hydration or lipid packing in the interface region.[38–40] As shown in Fig. 4B, the binding of polyarginine to LUV induced the decreases in the D_2O/H_2O fluorescence intensity ratio and WMF of dansyl-PE, and this trend was more significant for the longer polyarginine: the order of decrease in the D_2O/H_2O fluorescence intensity ratio and WMF was R8 ≈ PLA69 < PLA293 ≈ PLA554. These results suggest that polyarginine binds to the membrane interface region, with the degree of membrane insertion being greater for the longer polyarginine.

2.4. ITC measurements for binding of polyarginine to lipid membrane

To further compare the interaction of polyarginine with lipid membranes, isothermal titration calorimetry (ITC) measurements were employed. First, we measured the enthalpy of binding by injecting polyarginine into SBPL LUV at a low arginine/lipid molar ratio (< 1/2000). Fig. 5A shows the result of PLA554 injections into SBPL LUV. Because of the large lipid-to-arginine ratio, the injected PLA is likely to be almost completely bound to the membrane surface, and in fact the heats of consecutive injections were virtually identical. The obtained binding enthalpies, $\Delta H°$, expressed as kcal per mol or residual mol of polyarginine are summarized in Table. 1. In addition that the longer PLA exhibited much larger exothermic heat when compared per polymer molar basis, $\Delta H°$ values per arginine residue of PLA were still larger than R8. This indicates that the binding of PLA with longer chain to lipids is more exothermic process than the shorter polyarginine such as R8.

To obtain a comprehensive set of thermodynamic parameters for binding of polyarginine to lipids, further titration calorimetry for PLA554 injected into SBPL LUV was performed (Fig. 5B). In this condition, the enthalpy change of PLA554 binding to vesicles decreased with increasing the molar ratio of arginine to lipid, and the binding become saturated at high arginine-to-lipid ratio.

The binding isotherm of PLA554 to SBPL LUV was derived from the results in Fig. 5B as described.[41] In brief, the fraction of bound polyarginine for each injection, $f_{b,\,i}$, was calculated according to:

$$f_{b,\,i} = n_{b,\,i} / n_i = \Delta H_i / \Delta H° \qquad \text{(Eq. 2)}$$

where $n_{b,\,i}$ and n_i are the bound and injected molar amount of polyarginine, respectively, and ΔH_i is the i th enthalpy change for each titration. Then, the free polyarginine concentration, P_f, is expressed by

$$P_f = P_T - P_b = P_T - \sum_i f_{b,\,i} \times n_i \times 1000 / 1.3507 \qquad \text{(Eq. 3)}$$

where P_T and P_b are total and bound polyarginine concentrations after the *i* th injection, respectively. Now, binding of polyarginine to lipid vesicles is expressed by one-site binding model assuming that polyarginine binds to discrete, equivalent, and non-interacting binding sites on the membrane surface,

$$X_b = P_b / [\text{outer phospholipid}] = B_{max} P_f / (K_d + P_f) \quad \text{(Eq. 4)}$$

where [outer phospholipid] was taken as 54 % of the total phospholipid concentration, which corresponds to the theoretical fraction of lipid in the outer monolayer of spherical vesicles with a diameter of 100 nm and a bilayer thickness of 4 nm,[31] based on the assumption that polyarginine attaches only the outer leaflet of the SBPL bilayer due to the lack of evidence showing translocation of polyarginine across the LUV membranes.[30,31] K_d and B_{max} are the dissociation constant and the maximal binding capacity, respectively. Binding data were analyzed by the Hanes-Woolf equation:

$$P_f / X_b = K_d / B_{max} + P_f / B_{max} \quad \text{(Eq. 5)}$$

From the linear regression line shown in Fig. 5C, K_d and B_{max} values for polyarginine were obtained (Table 1). As shown in Fig. 5D, there was a good agreement between the experimental data and the theoretical binding isotherm calculated from the obtained K_d and B_{max} values.

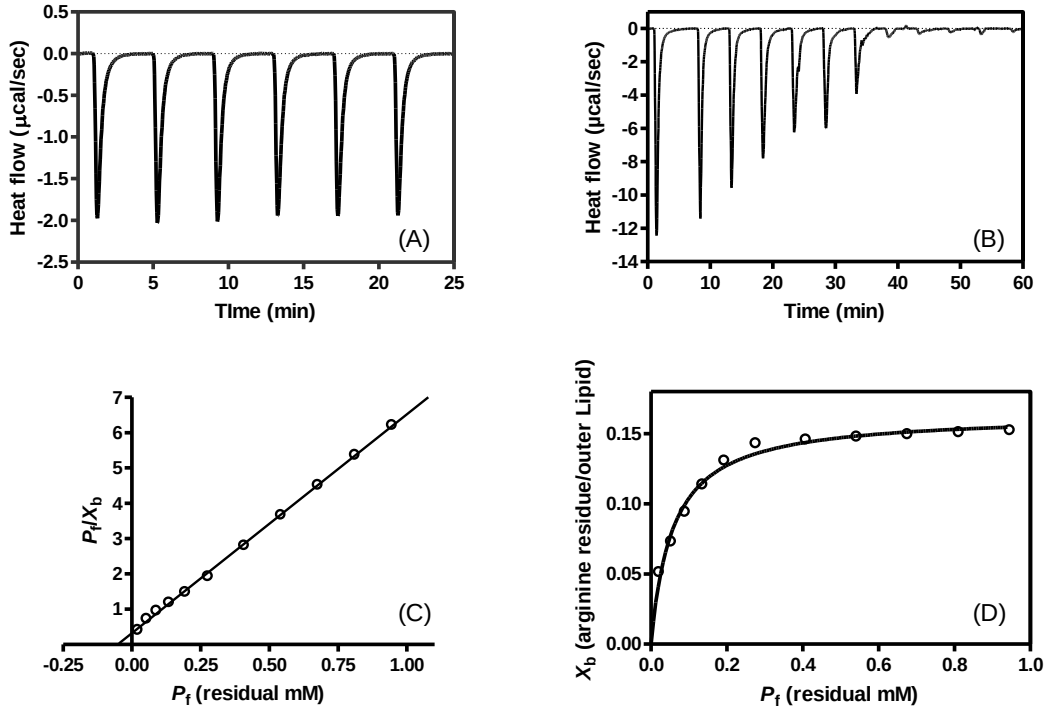

Fig. 5. (A) Isothermal titration calorimetry for PLA554 (5 residual mM) injected into SBPL LUV (10 mM). Each peak in heat flow chart corresponds to the injection of 5 µL aliquots of PLA554 at 25 °C. (B) Isothermal titration calorimetry for PLA554 (20 residual mM) injection into SBPL LUV (10 mM). Each peak in heat flow chart corresponds to the injection of 10 µL aliquots of PLA554 at 25 °C. (C) Hanes-Woolf plot for the binding data of PLA554 to LUV. (D) Binding isotherm of PLA554 to SBPL LUV from ITC data. The solid line is the theoretical binding isotherm calculated using Eq. 4 and parameters listed in Table 1. Reproduced in part with permission from *Langmuir* 2011, **27**, 7102-7103. © 2011 American Chemical Society.

Table 1. Thermodynamic parameters for binding of polyarginine to SBPL LUV. Reproduced in part with permission from *Langmuir* 2011, **27**, 7103. © 2011 American Chemical Society.

	B_{max} (residual mol/ mol outer lipid)	K_d (μM)	ΔG^o (kcal/mol)	ΔH^o (kcal/mol)	$T\Delta S^o$ (kcal/mol)
R8	0.13 ± 0.006	6.4 ± 0.28 (51 ± 2.2)	−9.5 ± 0.1 (−8.2 ± 0.1)	−7.4 ± 0.2 (−0.90 ± 0.03)	2.0 ± 0.2 (7.3 ± 0.05)
PLA69	0.16 ± 0.002	1.1 ± 0.01 (73 ± 1.0)	−10.5 ± 0.1 (−8.0 ± 0.1)	-1.1×10^2 ± 2.7 (−1.7 ± 0.03)	-1.0×10^2 ± 2.7 (6.4 ± 0.04)
PLA293	0.15 ± 0.003	0.26 ± 0.005 (75 ± 1.6)	−11.4 ± 0.1 (−8.0 ± 0.1)	-6.9×10^2 ± 23 (−2.4 ± 0.06)	-6.8×10^2 ± 23 (5.6 ± 0.07)
PLA554	0.16 ± 0.002	0.093 ± 0.001 (52 ± 1.0)	−12.0 ± 0.1 (−8.2 ± 0.1)	-1.3×10^3 ± 38 (−2.3 ± 0.05)	-1.2×10^3 ± 38 (6.0 ± 0.06)

Values in parenthesis are represented per arginine residue in polyarginine.

The Gibbs free energy $\Delta G°$ and entropy $\Delta S°$ for binding of polyarginine to LUV were calculated by the following equations:

$$\Delta G° = -RT \ln 55.5\left(1/K_d\right) \quad \text{(Eq. 6)}$$

$$T\Delta S° = \Delta H° - \Delta G° \quad \text{(Eq. 7)}$$

where the factor 55.5 represents the molar concentration of water and corrects for the *cratic* contribution to the binding event.[42] The resultant all thermodynamic parameters are summarized in Table 1. Although the binding parameters per polymer molar unit were quite different among polyarginines, the binding affinity (K_d) and the binding maximal capacity (B_{max}) per arginine residue unit are almost similar even including R8. In addition, the binding of polyarginine to lipids is enthalpically driven in which the $\Delta H°$ value greatly increases with increase in the chain length when analyzed by polymer molar unit. However, based on the analysis per arginine residue unit, the binding of polyarginine to SBPL LUV was found to be entropically driven in which the contribution

of enthalpy to the free energy of binding of polyarginine to lipids increases with increasing the chain length of polyarginine.

2.5. Translocation of polyarginine into giant vesicles

Confocal laser scanning microscopy measurements were performed to monitor the ability of polyarginine to translocate across SBPL membranes in giant vesicles. Fig. 6A shows the confocal laser scanning images of 5(6)-carboxyfluorescein (FAM)-labeled PLA293, 60 min after being added to giant vesicles, together with histograms of the relative fluorescence intensity between the periliposomal membrane region and the liposome inner phase (Fig. 6B). Fig. 6C summarizes the result of the statistical analyses for the differences in fluorescence intensity of FAM-labeled polyarginines between the inner and outer phases of giant vesicles. These results demonstrated that all polyarginines translocate into giant vesicles and the tendency of polyarginine to translocate membranes is on the order of R8 ≈ PLA69 < PLA293 ≈ PLA554. Interestingly, this order is consistent with the tendency to form α-helical structure upon lipid binding (Fig. 3) and the degree of insertion into the membrane interface region (Figure 4B) for polyarginine.

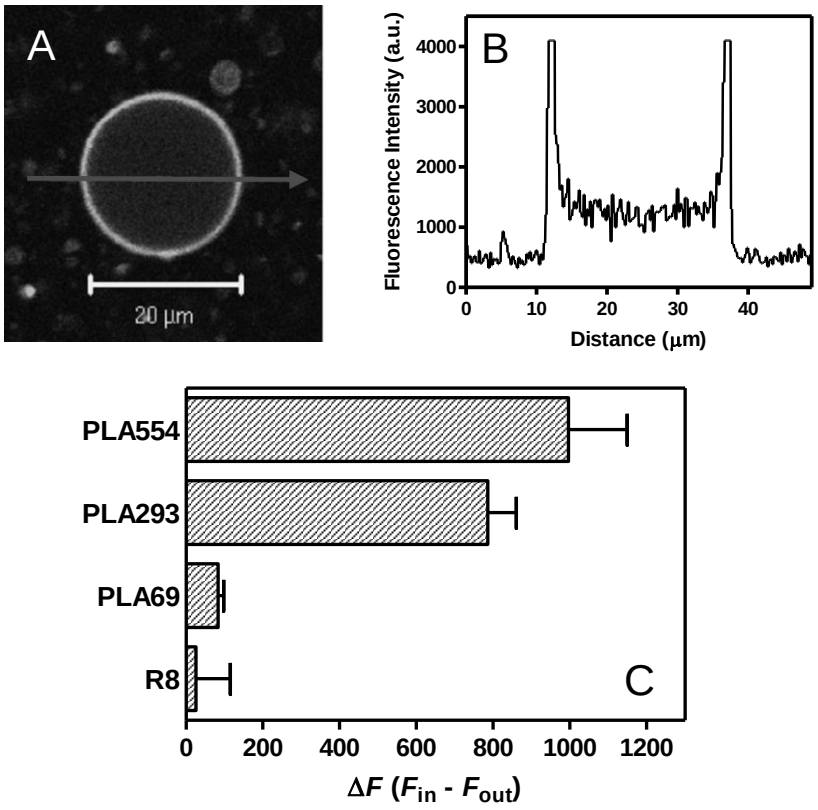

Fig. 6. (A) Confocal laser scanning images of FAM-labeled PLA293 added to SBPL giant vesicles (0.5 mM) at 60 min. (B) Histograms showing the relative fluorescence intensity between the periliposomal membrane region and the liposome inner phase. (C) The difference in FAM fluorescence intensity between the inner and outer phases of giant vesicles. The statistical analyses were taken from 5–10 vesicles. The concentrations of PLA and R8 were 0.3 and 0.015 residual mM, respectively. Reproduced in part with permission from *Langmuir* 2011, **27**, 7104. © 2011 American Chemical Society.

2.6. Mechanism of membrane penetration of polyarginine

Given that such structural changes of polyarginine from random coil to α-helix tend to occur for the longer chain polyarginines (Fig. 2B), the insertion of PLA293 or PLA554 into lipid membranes is expected to be more significant compared to R8 or PLA69 since the formation of intra- or inter-molecular hydrogen bonding of peptides drives the insertion of peptides into the interface or hydrocarbon regions of lipid membranes.[43] Supporting this, the hydration and packing of the membrane interface region is strongly affected by polyarginines (Fig. 4B), indicating that

polyarginine interacts with the membrane interface region. In addition, the finding that this interaction is greater for the longer polyarginine (Fig. 4B) suggests that the α-helix formation upon lipid binding facilitates the insertion of polyarginine into the membrane interface and causes the dehydration in this region.

Interestingly, there is same trend between the membrane perturbation and the ability of polyarginine to translocate lipid membranes in the order of R8 ≈ PLA69 < PLA293 ≈ PLA554 (Figs. 4B and 6). The free energy of transfer of PLA554 from water to the zwitterionic lipid bilayer interface is estimated to be 0.81×554 ≈ 449 kcal/mol of PLA since the Gibbs free energy of transfer of arginine residue from water to lipid bilayer interface is ~0.81 kcal/mol by the Wimley-White scales.[43,44] This indicates that despite of the large cost of the free energy of transfer to the hydrophobic environment polyarginine can translocate across the lipid membranes such that it binds to the lipid surface via electrostatic interactions, followed by the change in the secondary structure and the perturbation of the membrane structure. As a direct penetration mechanism of arginine-rich CPPs, recent experimental and molecular modeling analyses have proposed that the interaction of arginine-rich CPPs with lipid membranes induces the negative membrane curvature, leading to the formation of transient membrane pores.[45–51] It is possible that polyarginine moves across SBPL membranes via such a process, but the longer polyarginine such as PLA554 may have stronger effects on the membrane curvature than shorter polyarginine such as R8. In addition, it should be noted that despite small increases in α-helix content of PLA293 and PLA554 upon lipid binding, the α-helical residues of both PLA (13 and 60 arginines) are likely to be enough for the minimum length required for transmembrane helices.

ITC measurements demonstrated that binding of polyarginine to SBPL LUV is accompanied by a large exothermic heat (Fig. 5), indicating that the binding of polyarginine molecule to anionic lipid vesicles is enthalpically favorable (Table 1). Interestingly, based on the analysis per arginine residue

unit, the contribution of the enthalpy of the lipid binding of polyarginine to the free energy of binding increases with increasing the chain length of polyarginine whereas the free energy and the maximal capacity of binding are almost similar among all polyarginines (Table 1). In addition, the finding that the favorable enthalpy of binding of polyarginine to lipids increases from −0.9 to −2.4 kcal/mol of arginine residue depending upon the chain length of polyarginine (Table 1) suggest that the greater insertion of polyarginine into the membranes is enthalpically favorable process perhaps because it increases van der Waals interaction between polyarginine and membrane lipids.

To estimate the contribution of non-electrostatic interactions, i.e. hydrogen bonding, van der Waals interaction, hydrophobic interaction, to the binding of polyarginine to anionic vesicles, we treated the data with the surface partition equilibrium model (see Appendix).[52] Based on the data listed in Table 1, the non-electrostatic contribution to the binding free energy of polyarginine to SBPL LUV was estimated to be about −6 kcal/mol of arginine residue, corresponding to ~75 % of total free energy of binding of polyarginine: such a relatively large contribution of the non-electrostatic interaction to the binding of polyarginine to anionic vesicles has been also reported by other groups.[53,54] One possible explanation for the large non-electrostatic component in the lipid binding of polyarginine is the special hydrogen bonding properties of the guanidino group of arginine residue with phosphate group, which would facilitate a greater non-electrostatic interaction with the membrane interface layer. In this regard, in addition to the electrostatic interaction, non-electrostatic interactions such as hydrogen bonding, van der Waals interaction, and hydrophobic interaction, appear to play a role in the lipid binding and the membrane translocation processes of polyarginine as well as secondary structure of the polypeptides (Fig. 7).

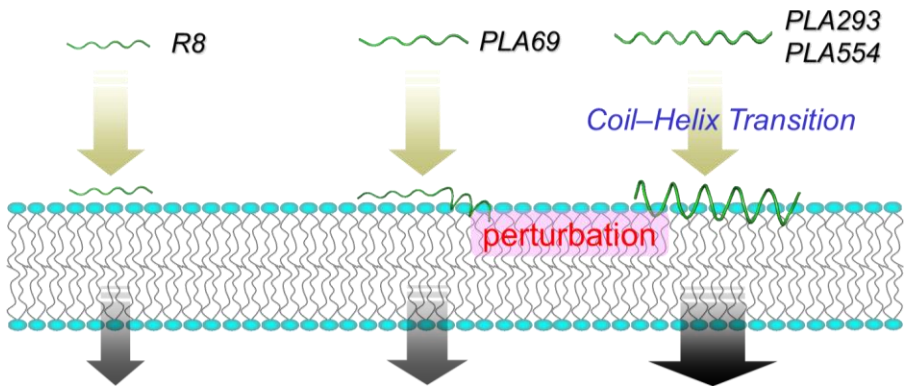

Fig.7. Proposed mechanism for membrane penetration of polyarginine. Positively charged polyarginines electrostatically bind to negatively charged lipid membrane, followed by non-electrostatic interaction with the lipid membrane in which hydrogen bonding, van der Waals interaction, and hydrophobic interactions occur. Such lipid interactions induce the transition from a random coil to the α-helix structure of the longer polyarginine, whereas no structural change was observed for the shorter polyarginine. As a result, the formation of α-helical structure upon lipid binding drives the insertion of polyarginine into the membrane interior, which enhances the membrane penetration of polyarginine. Reproduced in part with permission from *Langmuir* 2011, **27**, 7099. © 2011 American Chemical Society.

2.7. Stronger membrane interaction of polyarginine than polylysine

In this section, we made a comparative study of the interaction of PLA and PLL having similar chain length with lipid membranes. Described as previous section 2.6, the formation of intra- or inter-molecular hydrogen bonding of peptides drives the insertion of peptides into the interface or hydrocarbon regions of lipid membranes. CD measurements using 2,2,2-trifluoroethanol (TFE), which is used to examine the propensity to form α-helix structure of polypeptides,[55,56] clearly demonstrated that PLA293 has a greater propensity to form α-helix structure than PLL (Fig. 8A). In addition, ATR-FTIR (Fig. 9) spectral analyses indicate that the binding of PLA293 or PLL from the aqueous phase to the SBPL membrane results in the conformational transition to the α-helix structure in which the change in secondary structure of PLA293 is prior to PLL (Table 3). From these results, it is likely that PLA293 has a greater tendency to change the secondary structure upon lipid binding

than PLL. These results suggest that the degree of membrane insertion (or binding behavior) of polypeptides is dominated by not only electrostatic interactions but also the secondary structural change of polypeptides. It is plausible that the stronger interaction of arginine residue with negatively charged phospholipid membranes compared to lysine residue facilitates the conformational change in polypeptide, resulting in the peptide insertion into lipid membrane interior and the perturbation of the membrane structure.

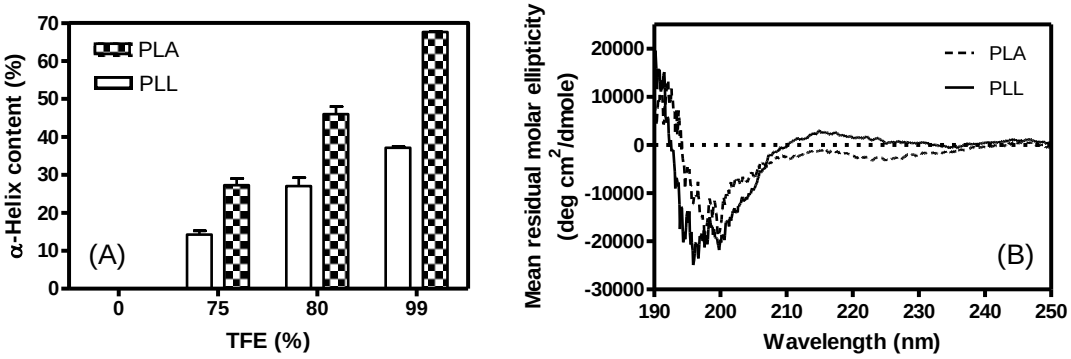

Fig. 8. (A) α-Helix contents of PLA293 (PLA) and PLL calculated from $[\theta]_{222}$ were plotted as a function of volume fraction of TFE. (B) Far-UV CD spectra of PLA293 (PLA) and PLL in the presence of SBPL LUV. The phospholipid concentration was 0.33 mM. The concentrations of PLA293 and PLL were 0.1 residual mM.

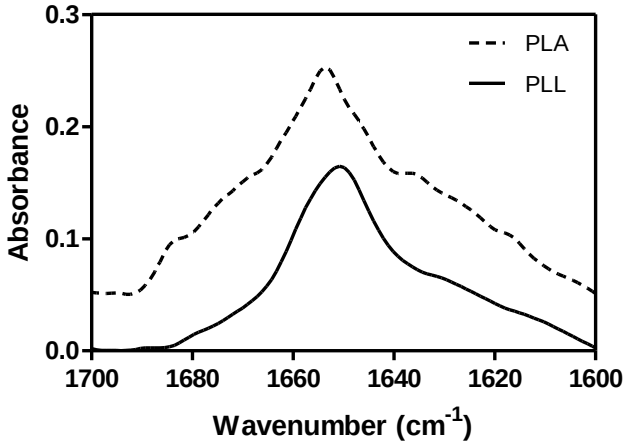

Fig. 9. ATR-FTIR spectra of PLA293 (PLA) or PLL bound to SBPL LUV.

Table 3. Frequencies and assignments of amide I component for PLA293 and PLL bound to SBPL LUV.

Assignment to secondary structure element	Frequency (cm^{-1})	Amide I component (%)	
		PLA293	PLL
α-helix	1655–1657	26	15
β-sheet	1624–1642 1691–1696	21	31
Contributions such as β-turn and side chain	1667–1685 1600–1618	38	7
random coil	1646–1650	15	47

ITC measurements demonstrated that the binding of PLA293 and PLL to SBPL LUV are accompanied by a large exothermic heat (Fig. 10), indicating that the binding of the positively charged polypeptides to anionic lipid membranes is enthalpically driven (Table 4). In addition, the contribution of the enthalpy of lipid binding of peptides to the free energy of binding was larger for PLA293 than PLL, whereas the free energy and the maximal capacity of binding are similar between PLA293 and PLL. Thus, compared to PLL, it is considered that the insertion of PLA293 into the membranes is more enthalpically driven through non-electrostatic interactions between PLA293 and membrane lipids, whereas this process is more entropically inhibited by the conformational constraint of PLA293 and lipid molecules on the membrane surface. Such an enthalpy-driven partitioning, referred to as the “non-classical” hydrophobic effect, appears to be a unique feature of solute-bilayer interactions and this behavior of arginine to lipid membranes was reported by other groups.

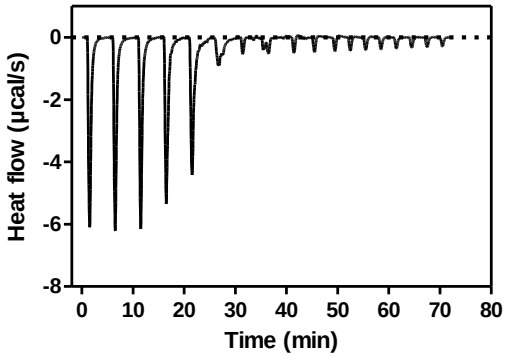

Fig. 10. ITC for PLL injection into SBPL LUV. Each peak in heat flow chart corresponds to the injection of 10 μL aliquots of PLL (20 residual mM) at 25 ℃. The phospholipid concentration of SBPL LUV was 10 mM.

Table 4. Thermodynamic parameters for the interaction of PLA or PLL with SBPL LUV obtained by ITC measurements[a]

	B_{max} (residual mol/ mol outer lipid)	K_d (μM)	ΔG^o (kcal/mol)	ΔH^o (kcal/mol)	$T\Delta S^o$ (kcal/mol)
PLA293[b]	0.15 ± 0.003	0.26 ± 0.005 (75 ± 1.6)	–11.4 ± 0.1 (–8.0 ± 0.1)	$-6.9\times10^2 \pm 23$ (–2.4 ± 0.06)	$-6.8\times10^2 \pm 23$ (5.6 ± 0.07)
PLL	0.15±0.001	0.12 ± 0.017 (33 ± 4.4)	–11.8 ± 0.1 (–8.5 ± 0.1)	$-3.1\times10^2 \pm 16$ (–1.2 ± 0.07)	$-3.0\times10^2 \pm 20$ (7.3 ± 0.08)

[a]Values in parenthesis are represented per amino acid residue in polypeptide.

[b]Data from Table 1.

Our finding of the more favorable enthalpy change in membrane interaction of PLA293 than PLL provides insights into the cell entry mechanism of CPPs, not only in the direct penetration, but also in the biological uptakes (i.e. endocytosis). To obtain therapeutic activity of delivered macromolecules using CPPs, the macromolecule-CPP complex has to be escaped from endosome by the CPP-lipid membrane interactions. The stronger enthalpy-driven partitioning of PLA293 with negatively charged lipids would induce the perturbation and destabilization of lipid membranes,

leading to the endosome disruption. Indeed, it is reported that the surface modification of lipid nanoparticles with octaarginine has a greater ability to escape from endocytic vesicles after cellular uptake compared to octalysine.[57]

2.8. Appendix

The surface partition equilibrium model considers that the charged peptide such as polyarginine partitions into the lipid membrane from the membrane surface without assuming a specific interaction between peptide and lipids. Therefore, the binding of polyarginine is described as the following equation:

$$X_{\mathrm{b}} = K_{\mathrm{p}} P_{\mathrm{s}} = K_{\mathrm{p}} P_{\mathrm{f}} \exp\left(-Z_{\mathrm{p}} F_0 \psi / RT\right) \tag{A1}$$

where K_{p} is the chemical partition coefficient, Z_{p} is the effective charge of the peptide, Ψ is membrane surface potential, F_0 is the Faraday constant, and RT is the thermal energy. The advantage of this model is that by replacing the bulk concentration of polyarginine (P_{f}) by its interfacial concentration (P_{s}), it can account for the enhanced surface concentration of polyarginine induced by the negative electrostatic potential of the lipid membrane. At the point of charge reversal (that is, ζ potential of the lipid membrane reaches zero), the surface concentration is identical to the bulk equilibrium concentration, which allows a straightforward estimation of the binding constant, K_{p}, as following equation[54]:

$$K_{\mathrm{p}} = X_{\mathrm{b}}^{\mathrm{sat}} / P_{\mathrm{s}}^{\mathrm{sat}} \tag{A2}$$

where $X_{\mathrm{b}}^{\mathrm{sat}}$ and $P_{\mathrm{s}}^{\mathrm{sat}}$ are the X_{b} and P_{s} when ζ potential equals zero, respectively. Subsequently, we can approximate the nonelectrostatic free energy of binding of polyarginine to lipids using the equation,

$$\Delta G_{\mathrm{nonel}} = -RT \ln 55.5 K_{\mathrm{p}} \tag{A3}$$

3. KINETICS OF NON-ENDOCYTOTIC MEMBRANE TRANSLOCATION OF OCTAARGININE BY REAL TIME IN-CELL NMR SPECTROSCOPY

3.1. Introduction

So far, no reports have succeeded in the quantitative observation of membrane translocation processes of CPPs *in situ*.[58] How much and how fast CPPs translocate into cell inside remains still unsolved. To well understand the translocation mechanism, it is crucial to establish the quantificational method without perturbing the system.

Almost all previous studies have relied upon the fluorescent labeling of CPPs or delivered cargo. Despite the high sensitivity, fluorophores strengthen the interaction of CPPs with lipid membrane,[50,51] induce photodamage of lipid bilayer membranes,[59] facilitate the uptake into the cell,[60] and modify the cellular distribution of the CPP.[61,62] Fluorophores change the structural flexibility and conformation of CPP.[63] Recently, an innovative MALDI TOF-MS quantification method using biotin-avidin interaction has been devoloped.[64–66] Although the biotinylated CPP as low as femtomole order has been quantified after incubation with cells, the method has missed the information about the real time processes of CPP uptake, rendering the kinetics of membrane translocation not available.

In this chapter, we develop a new methodology to quantify the kinetics of non-endocytotic membrane translocation of R8 peptide as CPP into natural living cells by using real time in-cell solution NMR spectroscopy. By introducing 4-trifluoromethyl-L-phenylalanine ($4CF_3$-Phe) to N terminus of R8, the direct membrane translocation of ^{19}F-labeled R8 (^{19}F-R8) into human myeloid

leukemia cells (HL60) is observed by ^{19}F NMR with a time resolution of minute-order. ^{19}F NMR is advantageous because it is sensitive and no backgrounds are present in the cell. It enables us to make a quantitative (concentration) analysis in relation to the molecular dynamics of biological interest without perturbing the system.[67–70] To validate our NMR kinetics study, we also confirmed the ^{19}F-R8 uptake to the HL60 cytosol using membrane solubilization and centrifugation techniques.

3.2. Real time in-cell ^{19}F NMR spectra measurement

Fig. 11A shows the real time in-cell ^{19}F NMR spectra of ^{19}F-R8 in PBS (0 min) and 4, 6, 8, 10, 12, 14 and 16 min after the addition to the HL60 cell at 4 °C, at which no endocytosis occur.[71] The signal at -62.20 ppm is assigned to the ^{19}F nucleus of 4CF_3-Phe at the N terminus of R8. It is found that the signal is broadened and moves to the low magnetic field within the first 4 min. We call it the state I. After 6 min, the signal comes back to the high field and becomes sharper (the state II). This is due to that the low field component gradually decreases in intensity during the period from 4 to 6 min. After 8 min, however, the peak top of the signal slightly moves to the lower field again (the state III). No further change is observed in the ^{19}F-R8 signal after 10 min and later.

As mentioned above, the time-dependent spectral changes in Fig. 11A imply that at least three different states of ^{19}F-R8 are present after the addition to the cell. It is convenient to see the difference spectrum to distinguish the states I, II, and III clearly. The difference spectrum analysis is useful in the present study because the integral intensity of ^{19}F-R8 is conserved all the time, meaning no degradation of ^{19}F-R8 occurred by the presence of HL60. By subtracting the spectrum of ^{19}F-R8 in PBS (0 min) from each spectrum after 4, 6, 8, 10, 12, 14 and 16 min with cell, we obtain the respective difference spectrum as shown in Fig. 11B.

The time course of the difference spectra shows that, actually, three components of ^{19}F-R8 appear after ^{19}F-R8 is added to the cell, in addition to the free component at -62.20 ppm. At first, the

two peaks are observed at -62.19 and -62.21 ppm after 4 min. These are finally assigned to ^{19}F-R8 that are bound to GAG (GAG) and ^{19}F-R8 interacting with the cell membrane (Membrane) in Fig. 11B. Afterwards, the third peak appears at -62.205 ppm after 6 min and increases in intensity after 8 min; see asterisk in Fig. 10B. We assign this peak to ^{19}F-R8 in cytosol (Cytosol) after crossing the membrane. It is noted that the above-mentioned peak assignments are reasonable in view of the following ^{19}F NMR observation. The first ^{19}F NMR result is that the chemical shift of ^{19}F-R8 moves toward the low magnetic field as compared to ^{19}F-R8 in PBS when ^{19}F-R8 is mixed with heparin; see Fig. 12A. Because heparin is frequently used as a model of GAG,[72–77] it is reasonable to assign the broad component at -62.19 ppm to ^{19}F-R8 that is bound to GAG. The assignment corresponds well with the previous consensus that R8 at first contacts GAG at the cell surface by the electrostatic interaction.[53] The second ^{19}F NMR observation is that the ^{19}F NMR signal moves to a high magnetic field where ^{19}F-R8 interacts with the lipid bilayer membrane, in contrast to the electrostatic ^{19}F-R8 binding to GAG. As illustrated in Figure 12B, we find that the ^{19}F-R8 signal shifts to a high field after the binding to large unilamellar vesicle of egg phosphatidylcholine (EPC) and egg phosphatidylglycerol (EPG). The result is consistent with the observation that the chemical shift of the ^{19}F NMR signal moves to the higher magnetic field when ^{19}F molecules are in a hydrophobic environment.[78–80] Thus we assign the peak at -62.21 ppm to ^{19}F-R8 in the membrane. Finally, it is reasonable to assign the third peak at -62.205 ppm (*) as ^{19}F-R8 in cytosol, considering that the peak comes back to the lower magnetic field because cytosol is a rather hydrophilic environment as compared to the cell membrane.

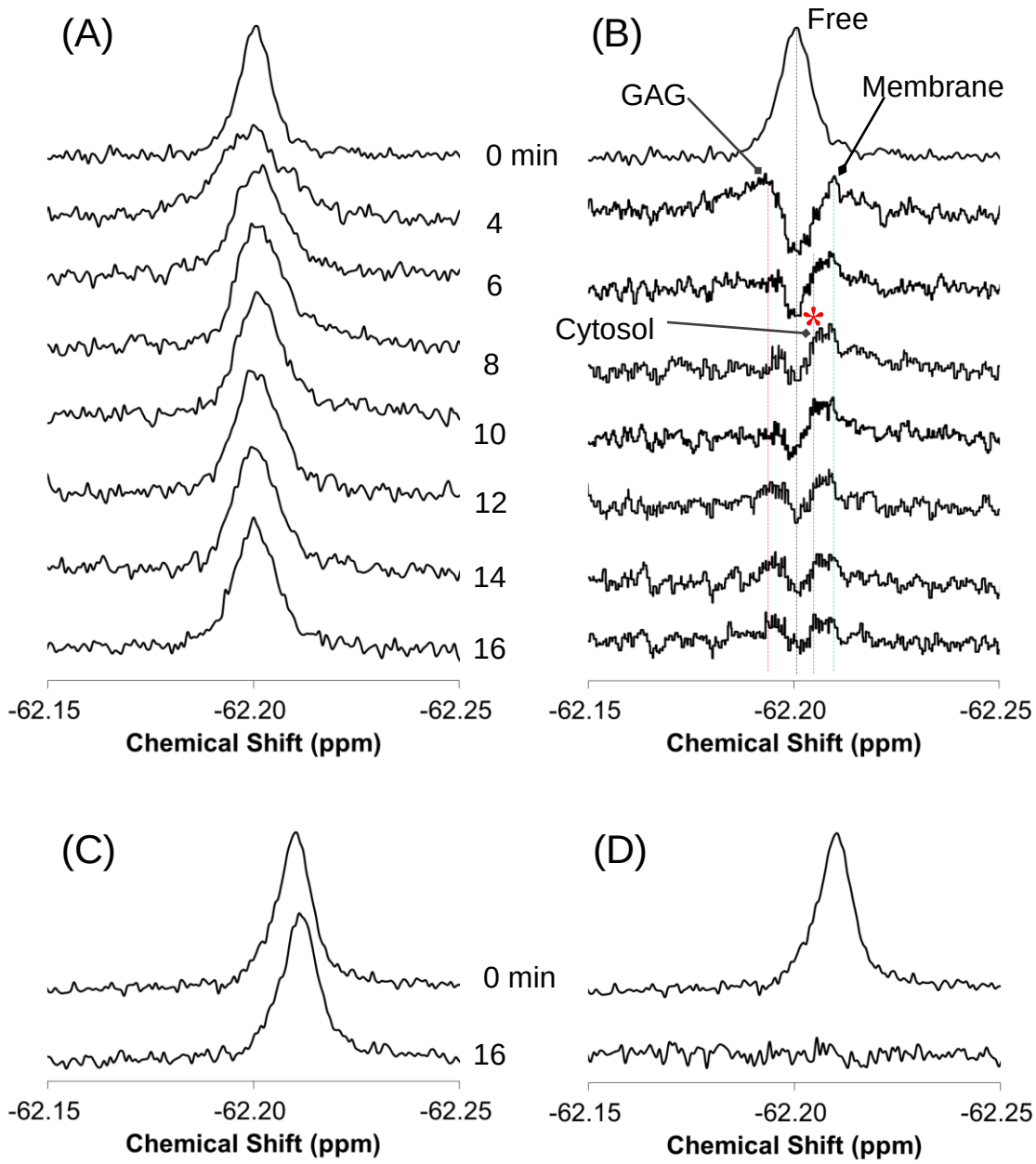

Fig. 11. Real time in-cell ^{19}F NMR (A) and difference spectra (B) of 80 μM ^{19}F-R8 in PBS (0 min), and 4, 6, 8, 10, 12, 14 and 16 min after the addition to HL60 at 4 °C. The top spectrum (Free) in (B) shows the ^{19}F NMR spectrum of ^{19}F-R8 in PBS (0 min). In (B), 4 components of ^{19}F-R8 in cell outside (Free), bound to GAG, bound to cell membrane (Membrane), and in cytosol (Cytosol) are designated by the dotted lines. Real time in-cell ^{19}F NMR (C) and difference spectrum (D) of 100 μM ^{19}F-T6 in PBS (0 min), and 16 min after the addition to HL60 at 4 °C. The upper spectrum in (D) shows ^{19}F-T6 in PBS (0 min).

To verify the reliability of the analysis, the real time in-cell ^{19}F NMR spectra of membrane-impermeable human lens αA-crystallin fragment called ^{19}F-T6 (TV-(4CF_3-Phe)-DSGISEVR) were also observed. As shown in Fig. 11C and 11D, no changes were found in the ^{19}F NMR spectrum nor the significant difference spectrum of ^{19}F-T6 even 16 min after the addition to HL60. The situation is a sharp contrast to ^{19}F-R8 where the translocation is already under equilibrium. The spectrum of ^{19}F-T6 was not changed even after 46 min (data not shown). The result demonstrates that no interaction occurs for ^{19}F-T6 in the presence of HL60. This is also supported by no spectral change of ^{19}F-T6 in the presence of heparin (Fig. 12C), indicating no binding to GAG at the HL60 cell surface.

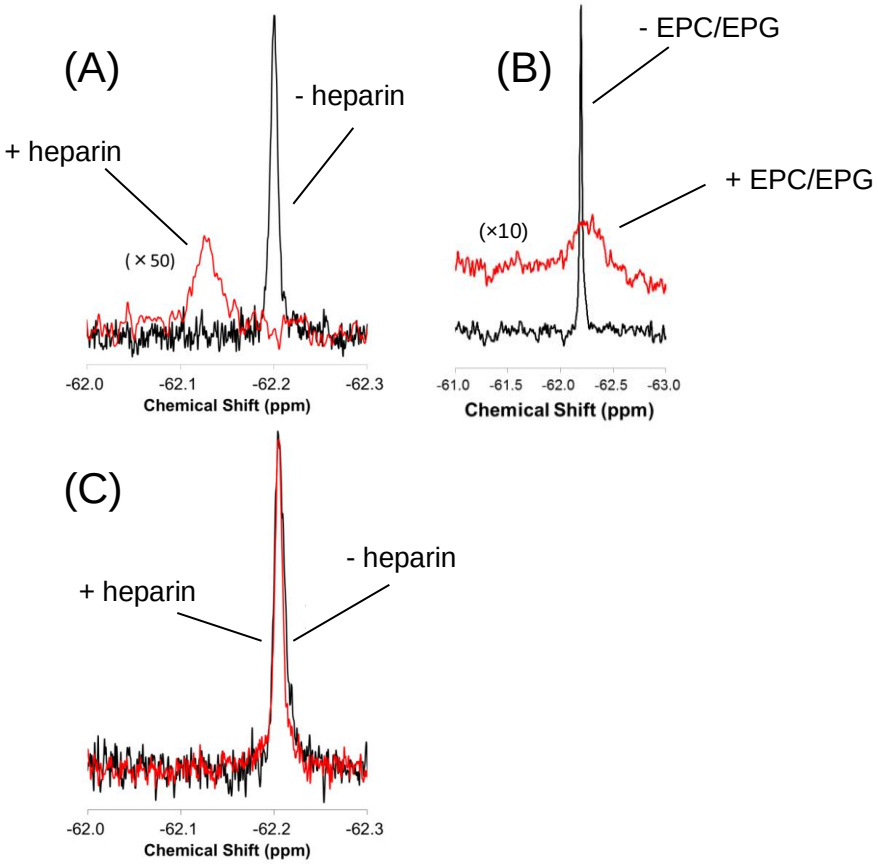

Fig. 12. ^{19}F NMR spectra of 80 μM ^{19}F-R8 in the presence and absence of 80 μM heparin (A) and 40 mM EPC/EPG bilayers (B) at 4 °C. The spectra of 100 μM ^{19}F-T6 in the presence of 200 μM heparin is also shown in (C) for comparison.

3.3. Kinetics of direct membrane translocation of ^{19}F-labeled octaarginine

In this section, we develop the kinetically-based procedure to analyze the non-endocytotic cell membrane translocation of ^{19}F-R8 *in situ*. By using the signal intensities of the real time ^{19}F NMR difference spectra (Fig. 11B), the quantities of four ^{19}F-R8 components, Free, GAG, Membrane, and Cytosol can be evaluated as a function of time. Fig. 13 quantifies how the concentration of each ^{19}F-R8 component varied after the addition to HL60.

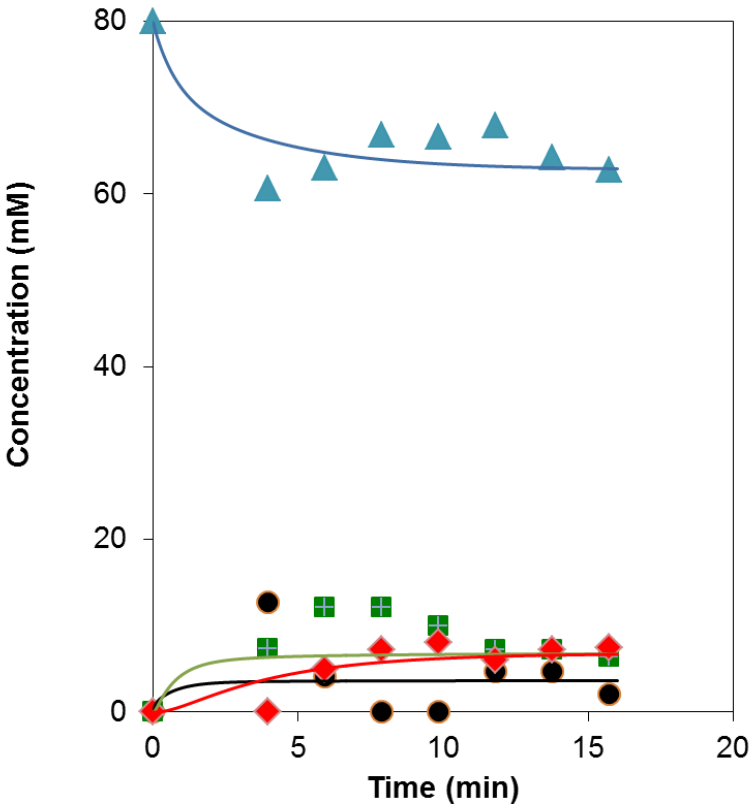

Fig. 13. Real time changes of ^{19}F-R8 concentrations in cell outside (Free, triangle), bound to GAG (circle), bound to cell membrane (square), and in cytosol (diamond) of HL60 at 4 °C. Symbols represent the experimental values. Solid lines are the calculated ones from the improved Euler method, by using the obtained rate constants k_1, k_{-1}, k_2, k_{-2}, k_3 and k_{-3} in Table 5.

Here, the kinetic model for the direct membrane translocation of ^{19}F-R8 could be written as,

$$\text{[Free]} \underset{k_{-1}}{\overset{k_1}{\rightleftarrows}} \text{[GAG]} \underset{k_{-2}}{\overset{k_2}{\rightleftarrows}} \text{[Membrane]} \underset{k_{-3}}{\overset{k_3}{\rightleftarrows}} \text{[Cytosol]}$$

where k_1, k_{-1}, k_2, k_{-2}, k_3 and k_{-3} are the rate constants of the ^{19}F-R8 binding to GAG (k_1), the dissociation from GAG (k_{-1}), entry from GAG to cell membrane (k_2), from membrane to GAG (k_{-2}), from membrane to cytosol (k_3), and from cytosol to the membrane (k_{-3}). According to this model, the respective fractions of ^{19}F-R8 should be given by the set of differential equations as,

$$\begin{aligned}
\frac{d[\text{Free}]}{dt} &= -k_1[\text{Free}] + k_{-1}[\text{GAG}] \\
\frac{d[\text{GAG}]}{dt} &= k_1[\text{Free}] - k_{-1}[\text{GAG}] - k_2[\text{GAG}] + k_{-2}[\text{Membrane}] \\
\frac{d[\text{Membrane}]}{dt} &= k_2[\text{GAG}] - k_{-2}[\text{Membrane}] - k_3[\text{Membrane}] + k_{-3}[\text{Cytosol}] \\
\frac{d[\text{Cytosol}]}{dt} &= k_3[\text{Membrane}] - k_{-3}[\text{Cytosol}]
\end{aligned} \qquad \text{(Eq. 8)}$$

where [Free], [GAG], [Membrane] and [Cytosol] are the concentrations of ^{19}F-R8 in PBS, bound to GAG, in membrane, and in cytosol, respectively. On the other hand, d[Free]/dt, d[GAG]/dt, d[Membrane]/dt, and d[Cytosol]/dt are given by derivation of the fitting curves in Fig. 13. Here, the fitting curves were calculated by using 4th to 6th-order polynomial equations with the range of $0 \le t \le 16\text{min}$. Also, we used the relations between k_1, k_{-1}, k_3, and k_{-3} at equilibrium as

$$-k_1[\text{Free}]_{\text{eq}} + k_{-1}[\text{GAG}]_{\text{eq}} = 0 \qquad \text{(Eq. 9)}$$

and

$$k_3[\text{Membrane}]_{\text{eq}} - k_{-3}[\text{Cytosol}]_{\text{eq}} = 0 \qquad \text{(Eq. 10),}$$

where $[\text{Free}]_{\text{eq}}$, $[\text{GAG}]_{\text{eq}}$, $[\text{Membrane}]_{\text{eq}}$ and $[\text{Cytosol}]_{\text{eq}}$ are the concentrations of the respective components in the equilibrium state ($t \ge 12\text{min}$). The rate constants k_1, k_{-1}, k_2, k_{-2}, k_3, and k_{-3} thus calculated are listed in Table 5.

Table 5. Rate constants ($k_{\pm i}$), equilibrium constants (K_i), and Gibbs energy changes (ΔG_i) in the membrane translocation processes of ^{19}F-R8 to HL60. Here *i* stands for the processes of ^{19}F-R8 binding to GAG (*i* = 1), from GAG to membrane (*i* = 2), and from membrane to cytosol (*i* = 3), respectively. The probability P_i of finding the *i* th system with the energy E_i at thermal equilibrium in canonical ensemble is also listed.

Process	$k_{\pm i}$ (min^{-1})	K_i	ΔG_i (kJ/mol)	E_i (kJ/mol)	$P_i \times 100$ (%)
Bound to GAG	k_1 0.19±0.04 k_{-1} 3.2±0.6	K_1 0.059	ΔG_1 6.5	E_1 6.5	P_1 5.6
GAG to membrane	k_2 7.5±2.0 k_{-2} 4.1±1.0	K_2 1.8	ΔG_2 -1.4	E_2 5.1	P_2 9.9
membrane to cytosol	k_3 0.31±0.06 k_{-3} 0.31±0.06	K_3 1.0	ΔG_3 0.0	E_3 5.1	P_3 9.9

From the results, it is found that the binding of ^{19}F-R8 to GAG is the slowest, with the rate constant k_1 at 0.19 min^{-1}. Although the binding to GAG is rate-limiting, the uptake to the lipid membrane proceeds most rapidly (k_2 at 7.5 min^{-1}). This is because the positive charge of R8 will be cancelled by the anionic GAG at the cell surface. In contrast, the entry into cytosol from the membrane is more than one order of magnitude as slow as the penetration into the membrane, as demonstrated by the rate constant k_3 at 0.31 min^{-1}. It should be noted that the reverse movement from cytosol to the membrane occurs as frequently as the entry into the cytosol; notice that the rate constants k_{-3} and k_3 are found to be equal within the experimental error. The plausible mechanism of R8 entry into cytosol across the membrane will be described later in detail.

To confirm the validity of the obtained rate constants, we attempted to calculate the time course of the concentrations of each R8 component numerically by using the obtained rate constants k_1, k_{-1}, k_2, k_{-2}, k_3 and k_{-3} in Table 5. For the numerical calculation, the improved Euler method was applied. In Fig. 13, the calculated variations of the respective R8 concentrations are also shown as the solid lines. Each line is found to approximately reproduce the experimental values of R8 concentrations as a function of time, by which the reliability of the present analysis is shown.

For a better understanding of the mechanism of ^{19}F-R8 translocation into HL60, the equilibrium constants, $K_i = k_i/k_{-i}$ and the Gibbs energy changes, ΔG_i for the ith process (i = 1, 2, and 3) are estimated and listed in Table 5. Obviously, the uptake of ^{19}F-R8 from GAG to membrane is energetically favorable (ΔG_2 = -1.4 kJ/mol). The neutralization of cationic ^{19}F-R8 by the negatively charged GAG accelerates the insertion into the cell membrane via non-electrostatic interactions such as hydrogen bonding, van der Waals force, and the hydrophobic effect as discussed in chapter 2.

Table 5 also shows that no energy is required for the translocation from membrane to cytosol (i= 3). No energy difference was found between ^{19}F-R8 in the membrane and in the cytosol. This is closely related to the translocation mechanism that R8 spontaneously induces the negative membrane curvature to enter cytosol easily through the water-abundant part of the membrane, the detail of which will be discussed later.

The kinetic results are further validated by using the Boltzmann population formula (Eq. 11):

$$P_j = \frac{\exp(-E_j / RT)}{\sum \exp(-E_j / RT)} \qquad \text{(Eq. 11)}$$

This equation expresses the probability P_j of finding the j th system with the energy of E_j at thermal equilibrium in canonical ensemble. The denominator is called as the partition function. With the free state of ^{19}F-R8 outside HL60 as the reference, Eq. 11 can be rewritten as

$$P_i = \frac{\exp(-E_i / RT)}{1 + \sum \exp(-E_i / RT)} \qquad \text{(Eq. 12)}$$

In Eq. 12, the statistical weight of the ^{19}F-R8 outside HL60 is 1, that means E = 0, and i (= 1, 2, and 3) corresponds to the process of ^{19}F-R8 translocation as listed in Table 5. Under these conditions, E_i is derived from the values of ΔG_i (Table 5). Moreover, we can calculate the amounts of ^{19}F-R8 bound to GAG, bound to membrane, and in cytosol of HL60 at equilibrium by assigning i = 1, 2 and 3 to Eq. 12, respectively.

It is found that the probabilities of ^{19}F-R8 lying in the respective processes of translocation, P_1, P_2, and P_3 are 5.6, 9.9, and 9.9%, respectively (Table 5). Since the total amount of ^{19}F-R8 is 80 μM, this means that 4.5 μM of ^{19}F-R8 is bound to GAG, 7.9 μM of ^{19}F-R8 is penetrated into the membrane, and 7.9 μM of ^{19}F-R8 is translocated into cytosol under equilibrium. These values are in good agreement with the experimental ones in Fig. 13 in the equilibrium state ($t \geq 12$ min).

Our findings suggest that the direct translocation probability of ^{19}F-R8 is low due to impaired membrane fluidity at 4 °C. In fact, we have recently clarified that the protrusion of phospholipids, which is the fluctuation of the molecules in the vertical direction to the membrane lipid bilayer surface, is inhibited in the fluid phase at low temperature. From this point of view, the membrane fluctuation is crucial for the direct membrane translocation of CPPs, and the membrane perturbation such as transient toroidal pore generation in cell membrane for the mechanism is feasible.

3.4. Distribution of ^{19}F-labeled octaarginine after cell membrane solubilization and centrifugation

In the previous section, we have succeeded in analyzing the kinetics of the non-endocytotic translocation of ^{19}F-R8 to the cell inside. It is crucial, however, to confirm that ^{19}F-R8 is actually transferred to the HL60 cytosol across the cell membrane. For this purpose, the final distribution of

^{19}F-R8 was evaluated after equilibrium was attained in the real time NMR measurement. Membrane solubilization and centrifugation techniques were combined in accordance with the scheme 1.

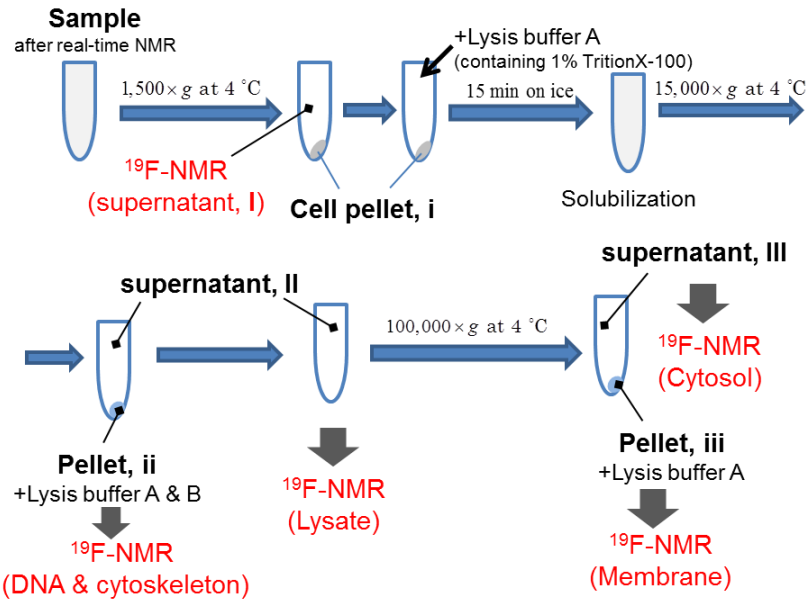

Scheme 1. Solubilization and centrifugation procedures for steady-state NMR measurements.

First, we examined how much of ^{19}F-R8 was finally bound to the cell. In Fig. 14A, the ^{19}F NMR spectra of ^{19}F-R8 in the supernatant **I** after the centrifugation is compared with total ^{19}F-R8 as a control. The ^{19}F NMR signal intensity of the supernatant corresponds to ^{19}F-R8 that is still in a free (unbound) state under equilibrium. It is found that 77 % of ^{19}F-R8 was in a free state. The value is consistent with the result of the real time in-cell NMR spectra showing about 75% (60 μM) of ^{19}F-R8 is remaining in a free state after the equilibrium is attained (Fig. 13). Next, to confirm that ^{19}F-R8 is actually bound to HL60 cell, the cell pellet **i** was solubilized by lysis buffer containing 1% Triton X-100. After the centrifugation, the supernatant **II** was subject to ^{19}F NMR measurement. The spectrum is shown in Fig. 14B as Lysate, and 13% of the initial ^{19}F-R8 was detected.

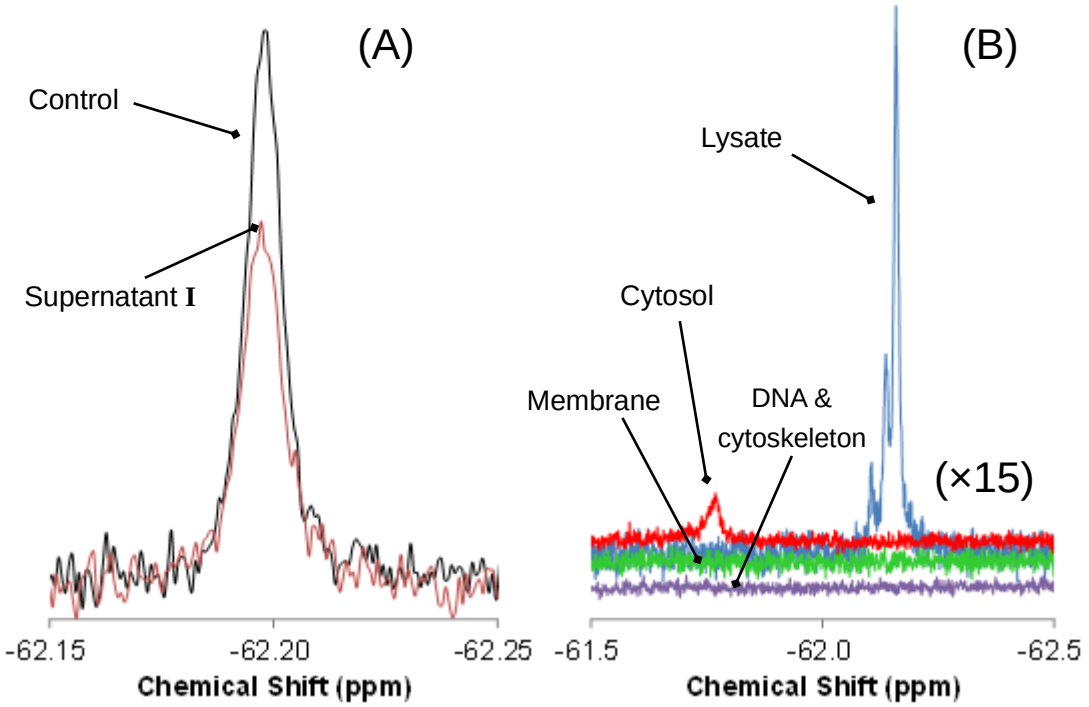

Fig. 14. (A) ^{19}F NMR spectra of ^{19}F-R8 in PBS (Control) and the supernatant **I** after the real time in-cell ^{19}F NMR measurement. (B) ^{19}F NMR spectra of ^{19}F-R8 fractions separated by solubilization and centrifugation in accordance with Scheme 1.

It is considered that 3 components of ^{19}F-R8 are contained in the Lysate. They include ^{19}F-R8 bound to GAG, ^{19}F-R8 bound to lipid membrane, and ^{19}F-R8 in cytosol. We selected these components as the supernatant **III** and the pellet **iii** by centrifuging the Lysate at 100,000×g. The former consists of ^{19}F-R8 in cytosol, and the latter ^{19}F-R8 bound to GAG or the lipid membrane; see Scheme 1. The ^{19}F NMR spectrum of the supernatant **III** shows that the signal of ^{19}F-R8 is observed in the cytosol fraction; see Fig. 14B. The result is valuable because it demonstrates the permeation of ^{19}F-R8 to the cytosol through the HL60 membrane. On the other hand, the ^{19}F-R8 in the membrane fraction is found to be within the experimental error at an equilibrium state.

As ^{19}F-R8 is cationic, it is possible that ^{19}F-R8 is finally bound to DNA in the HL60 nucleus. We

explored whether ^{19}F-R8 was bound to DNA or cytoskeleton by solubilizing the pellet **ii** in accordance to Scheme 1. As shown in Fig. 14B, the ^{19}F NMR signal of ^{19}F-R8 was undetectable in the DNA & cytoskeleton. This may be due to that the binding of ^{19}F-R8 to cellular component is too tight to solubilize by Triton X-100. In such case, the intensity of the NMR signal is underestimated by the signal broadening. Now, our theoretical calculation for the amount of the translocation into cytosol of ^{19}F-R8 is validated with experimental quantification by HL60 membrane solubilization and centrifugation technique. Our findings also suggest that direct translocation probability of ^{19}F-R8 is low due to impaired membrane fluidity at 4 °C. In fact, we have recently clarified that the protrusion of phospholipids, which is the fluctuation of the molecules in the vertical direction to the membrane lipid bilayer surface, is inhibited in the fluid phase at low temperature.[81]

3.5. Mechanism of non-endocytotic translocation of octaarginine

In this chapter, the real time in-cell NMR spectroscopy was applied to quantify kinetics of non-endocytotic membrane permeation of R8 as a CPP into natural living cells. The ^{19}F NMR successfully detected the real time R8 translocation: the binding to glycosaminoglycan (GAG) at the cell surface, followed by the penetration into the cell membrane, and the entry into the cytosol after crossing the membrane. The kinetics showed the slow binding of R8 to GAG with the rate constant at 0.19 min^{-1}. Once the cationic nature of R8 was cancelled by anionic GAG, however, the uptake to the lipid membrane proceeded most rapidly (7.5 min^{-1}). In contrast, the rate constant of the entry into cytosol was 0.31 min^{-1}, more than one order of magnitude as slow as the penetration into the membrane. Almost no energy was required, however, for the entry of cationic R8 into cytosol across the hydrophobic membrane. These results suggest that the mechanism for non-endocytotic membrane translocation of cell-permeable octaarginine is transient toroidal pore model (Fig. 15). Note that, the lifetime of the transient pore formed by CPPs is much lower than that of toroidal pore

formed by cytotoxic amphiphatic antimicrobial peptides.[82–84] Thus, it is known that CPPs do not exhibit the cytotoxicity.[2,85,86] Consistent with this, no cell cytotoxicity, assessed by the trypan blue staining after the NMR measurement, was observed as descried in section 6.9.

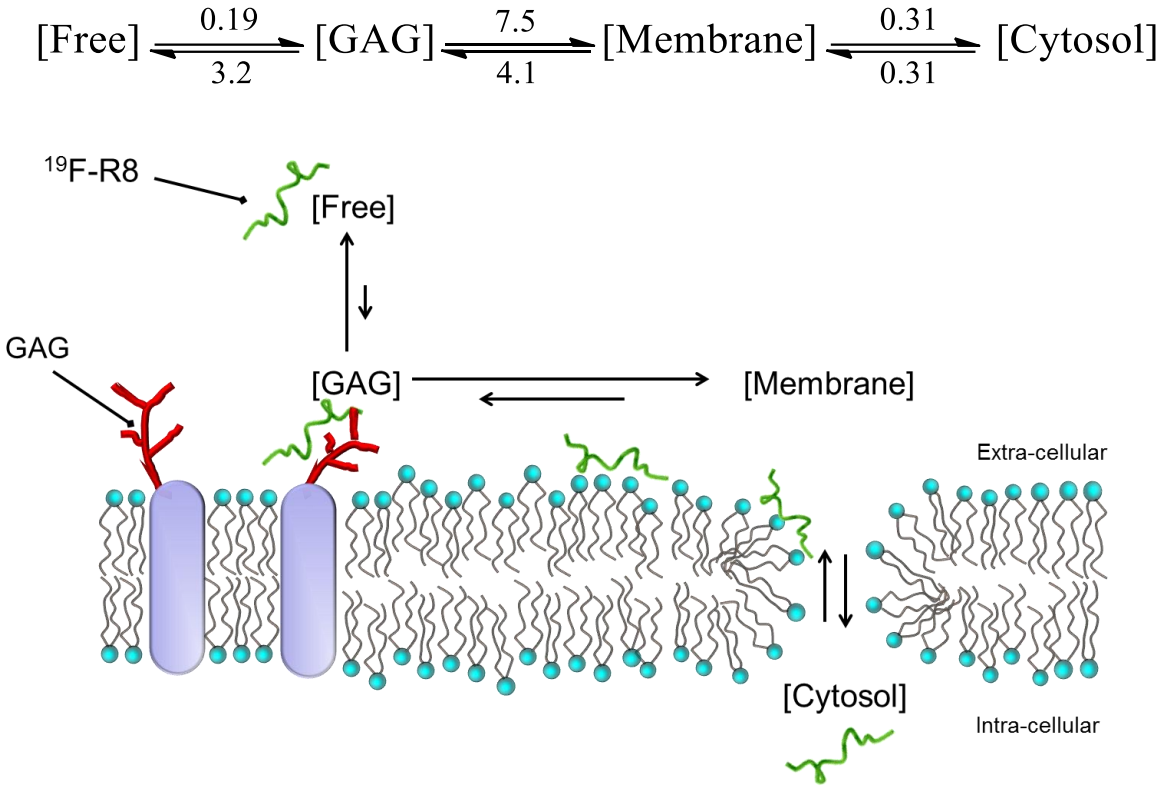

Fig. 15. The kinetic model and proposed mechanisms for the non-endocytotic direct membrane translocation of ^{19}F-R8. The mechanism of ^{19}F-R8 translocation into cell is considered as: the binding to glycosaminoglycan (GAG) at the cell surface, followed by the penetration into the cell membrane, and the entry into the cytosol with transient destabilization of lipid membrane to enter cytosol easily through the water-abundant part of the membrane.

4. CONCLUSIONS

Although non-endocytotic direct cell membrane translocation is considered as an alternative to endocytosis, the internalization mechanism of cationic CPPs across hydrophobic cell membranes is still controversial. In this thesis, the mechanism of membrane penetration of polyaginine was investigated from physicochemical aspects.

The results in chapter 2 demonstrated that polyarginine binds to the membrane interface region, with the degree of insertion being greater for the longer polyarginine. Such lipid interaction induces the transition from a random coil to the α-helix structure of the longer polyarginine whereas no structural change was observed for the shorter polyarginine. In addition, favorable enthalpic contribution to the energetics of lipid binding of polyarginine increases with the increase in the polymer chain length. On the basis of these observations, it appears that the enhanced ability of the longer polyarginines to translocate lipid membranes is due to their greater perturbation of the membrane structure. Thus, the formation of α-helical structure upon lipid binding drives the insertion of polyarginine into the membrane interior, which enhances the membrane penetration of polyarginine.

To our best knowledge, real time in-cell NMR study in chapter 3 is the first report demonstrating the quantitative physical parameters for the direct translocation process of cell penetrating ^{19}F-R8 in cells *in situ*. Our methodology quantitates the rate constant, equilibrium constant, change in Gibbs energy, and even the amount of transmitted CPP into cytosol of HL60 cells. Our theoretical calculation for the amount of the translocation into cytosol of ^{19}F-R8 is also consistent with experimental quantification. Based on these results, the mechanism of octaarginine translocation into cell is considered as follows: octaarginine binds to glycosaminoglycan at the cell surface, followed by the penetration into the cell membrane with transient destabilization of membrane structure, resulting in entry into cytosol easily through the water-abundant part.

5. MATERIALS

Poly-L-arginine (PLA) hydrochloride with averaged degree of polymerization determined by viscosity measurements of 69, 293, or 554 (averaged molecular weight is 13,300, 56,400, or 106,800, respectively), Poly-L-lysine hydrobromide with averaged degree of polymerization determined by viscosity measurements of 266 (averaged molecular weight is 55,600), soybean phospholipid (SBPL) and dipalmitoylphosphatidylglycerol (DPPG) were purchased from Sigma-Aldrich (Japan). SBPL contains phosphatidylcholine (40%), phosphatidylethanolamine (30%), phosphatidic acid (15%), phosphatidylinositol (4%), cardiolipin (5%), and others. Egg phosphatidylcholine (EPC, >96% pure) and egg phosphatidylglycerol (EPG, >95% pure) were obtained from NOF CORPORATION (Tokyo, Japan). Heparin sodium salt (from porcine intestinal mucosa; average molecular weight, 18,000 Da) was purchased from SIGMA (St. Louis, MO). Diphenyl-1,3,5-hexatriene (DPH), 1-[4-(trimethylamino]phenyl]-6-phenylhexa-1,3,5-triene (TMA-DPH), and dansyl-PE were purchased from Molecular Probes (Eugene, OR). 2,4-Bis-(*N*,*N*'-di(carboxymethyl)aminomethyl)fluorescein (calcein) and 5-(and 6-)-carboxyfluorescein (FAM) succinimidyl ester were purchased from Invitrogen (Carisbad, CA). Octaarginine (R8), FAM-labeled R8, and ^{19}F-labled R8 were synthesized manually by Fmoc solid-phase chemistry as described.[87] A fragment peptide, called ^{19}F-T6 (TV-(4CF_3-Phe)-DSGISEVR), from human lens αA-crystallin[88] was synthesized by Fmoc solid-phase chemistry using an automated solid-phase synthesizer (PSSM-8; Shimadzu, Kyoto, Japan). The purity of each peptide was confirmed to be >95% by reversed-phase high-performance liquid chromatography and mass spectrometry. All other reagents were special grade and used without further purification.

6. METHODS

6.1. FAM Labeling Procedure

PLA was labeled with FAM according to the protocol as below. 10 mg/mL of PLA solution in 10 mM sodium bicarbonate buffer (pH 9.0) was coupled with FAM overnight. The resultant FAM-PLA was separated from the free FAM by exclusion chromatography using a Sephadex G-25 column by eluting in 10 mM Tris-HCl buffer (pH 7.4).

6.2. Liposome Preparation

SBPL was dissolved in chloroform in a round-bottomed flask and dried under a stream of N_2 gas to produce a thin, homogeneous lipid film. For giant vesicle preparation, the dried lipid film was gradually hydrated with 10 mM Tris-HCl buffer for more than 24 h at 4 °C to be stripped off the glass surface. The obtained giant vesicle suspensions were centrifuged at 13,000 rpm for 10 min to remove contaminating multilamellar vesicles.[89] For LUV preparation, the lipid film was voltexed in Tris buffer to obtain multilamellar vesicle suspension. The resultant suspension was subjected to five cycles of freeze-thawing and was then passed through a Mini-extruder equipped with two stacked 0.1 μm polycarbonate filters (Avanti, Alabaster, AL). The phospholipid concentration was determined by the Bartlett method.[90] Averaged particle size of 110–120 nm and ζ potential of –25 mV for LUV were confirmed using NICOMP 380ZLS potential/particle sizer (NICOMP, Santa Barbara, CA).

6.3. Circular Dichroism (CD) Spectroscopy

Far-UV CD spectra were recorded from 190 to 250 nm at 25 °C using a J-600 CD spectropolarimeter with a 2 mm quartz cuvette. Polyarginine sample was diluted to 0.3 residual mM in 10 mM Tris-HCl buffer to obtain the CD spectrum. For the polyarginine- or

polylysine-LUV mixture, the polypeptides were incubated with LUV for 1 h prior to measurements. The spectrum was corrected by subtracting the buffer baseline or a blank sample containing an identical concentration of LUV. The α-helix content (%) of polypeptide was determined from mean residue ellipticity [θ] at 222 nm as described by Scholtz *et al.*[91]:

$$\alpha\text{-helix content (\%)} = \frac{[\theta]_{222} - [\theta]_{coil}}{[\theta]_{helix} - [\theta]_{coil}} \times 100 \quad \text{(Eq. 13)}$$

$$[\theta]_{helix} = -40000(1 - 2.5/n) + 100t$$

$$[\theta]_{coil} = 640 - 45t$$

where $[\theta]_{222}$ is the measured mean residue ellipticity at 222 nm expressed in degree cm^2 $dmol^{-1}$, $[\theta]_{helix}$ and $[\theta]_{coil}$ are the mean residue ellipticities of the completely helical and coiled forms of the polypeptide (at 222 nm, expressed in degree cm^2 $dmol^{-1}$), respectively, *n* is the number of amino acid residues, and *t* is the temperature in °C.

6.4. Attenuated total reflection-Fourier transform infrared (ATR-FTIR) spectroscopy

Samples prepared by adding PLA293 or PLL to SBPL LUV at ~0.1 amino acid/lipid molar ratio were centrifuged at 15,000 rpm for 1 h to remove the free peptides and deposited on germanium used as the waveguide. ATR-FTIR spectra were recorded over the wave number range of 1,000–3,500 cm^{-1} at a resolution of 4 cm^{-1} and 256 readings using a FTIR spectrometer FT/IR-4200 (JASCO). Secondary structure of PLA or PLL bound to SBPL LUV was analyzed by a Spectra Manager Software (JASCO).

6.5. Fluorescence Study

All fluorescence measurements were carried out using a Hitachi F-4500 fluorescence spectrophotometer. For steady-state fluorescence measurements, LUV was labeled with DPH or TMA-DPH by adding small aliquots of stock solution of probes in DMF to yield phospholipid:probe molar ratio of 200:1 or 100:1, respectively. For the sample labeled with dansyl-PE, SBPL and dansyl-PE were mixed in chloroform at a phospholipid:probe molar ratio of 200:1 before preparation of LUV. For the fluorescence anisotropy experiments, we measured fluorescence intensity (I) of $I_{0\text{-}0}$, $I_{0\text{-}90}$, $I_{90\text{-}0}$, and $I_{90\text{-}90}$, where the affixing character in the lower right of I indicates the direction of the plane of polarization of the polarizer and the analyzer. For example, $I_{0\text{-}0}$ and $I_{0\text{-}90}$ are the fluorescence intensities detected through a polarizer oriented parallel and perpendicular to the direction of polarization of the excitation beam. Fluorescence anisotropy, r, is given by

$$r = \frac{I_{0-0} - G\, I_{0-90}}{I_{0-0} + 2G\, I_{0-90}} \qquad \text{(Eq. 14)}$$

where $G = I_{90\text{-}0}/I_{90\text{-}90}$. DPH and TMA-DPH were excited at 360 nm and the fluorescence was detected at 430 nm. Dansyl-PE was excited at 336 nm and the fluorescence was detected at 513 nm. To evaluate water penetration into the membrane interface, the deuterium isotope exchange measurements were performed by monitoring emission spectra of dansyl-PE in D_2O buffer and comparing it to that in H_2O buffer from 450 to 600 nm at the excitation wavelength of 336 nm. The D_2O/H_2O fluorescence intensity ratio is calculated from integrated intensity of emission spectra from 500 to 550 nm in D_2O and H_2O buffer.

6.6. Isothermal Titration Calorimetry (ITC) Experiment

ITC measurements were carried out on a Microcal MCS ITC calorimeter. SBPL LUV was placed in the 1.3507 mL reaction cell, and a solution of polypeptide placed in a 250 μL titration syringe was injected into the LUV in cell. Prior to the measurements, the peptide solution and vesicle suspension were degassed under vacuum for 10 min. The injections were performed automatically at 25 ℃ under 400 rpm stirring. Binding enthalpies of polypeptide to LUV were corrected for heats of polypeptide dilution and dissociation; these values were determined by titrating polypeptide into buffer alone.

6.7. Confocal Laser Scanning Microscopy

The laser scanning confocal imaging system (Zeiss, LSM-410) equipped with an argon laser was used for confocal laser scanning microscopy. The fluorescence of FAM-labeled polyarginine was excited at 488 nm and the emission was observed through a band filter (515-565 nm). Samples were prepared by mixing giant vesicles and FAM-labeled polyarginine in a glass bottom dish (Matsunami Glass Ind., Osaka, Japan) at a ratio of PLA or R8 to lipid (arginine residue/mol of phospholipid) of 0.6 or 0.03, respectively. To prevent photo bleaching, the confocal microscope was operated under conservative laser intensity and time exposure conditions.

6.8. Real time in-cell ^{19}F NMR measurement

One-dimensional (1D) in-cell ^{19}F NMR measurements were carried out at 376.2 MHz by using a JEOL ECA400 NMR spectrometer equipped with a superconducting magnet of 9.4 T. A multinuclear probe (JEOL, NM40T10A/AT) for the 10-mm diameter tube was used. Detailed procedures of the measurement are described elsewhere (37). Briefly, HL60 from human promyelocytic leukemia (the

final concentration, 1×10^7 cells/ml, generous gift of Dr. Tohyama) was suspended in phosphate-buffered saline (PBS, pH 7.4) at 4 °C and put into a NMR tube. To avoid the cellular toxicity, D_2O amount used for the signal lock was decreased to 10%. The sample was gently rotated to prevent the sedimentation of the cell. The field-gradient shimming was applied before the addition of the peptide, to quickly attain the spectral resolution. The measurements started immediately after the thermal equilibrium is attained, 1.5 min after the addition of the ^{19}F-labeled peptides. The final concentrations of ^{19}F-R8 and ^{19}F-T6 were 80 μM and 100 μM, respectively, high enough to observe non-endocytotic translocation. Free induction decays (FIDs) were accumulated at 16 time/2 min intervals. The spectra were processed by the JEOL DELTA software. Chemical shift of the ^{19}F NMR signal was obtained by referring to the absorption frequency of the trifluoroacetic acid in the solvent. Cell viability, assessed by the trypan blue staining after the NMR measurement, was 92-93% for ^{19}F-R8 and 93-95% for ^{19}F-T6 with respect to the control value, 93-94%.

6.9. Steady state ^{19}F NMR measurement

The amount of ^{19}F-R8 finally delivered to the cytosol was quantified by ^{19}F NMR under equilibrium in combination with the cell membrane solubilization and centrifugation. The procedures are summarized in Scheme 1. After the real time ^{19}F NMR measurement, 4 ml of the sample were centrifuged at 1,500×g for 5 min at 4 °C. The pellet, **i** was washed again with 4 ml of PBS and centrifuged again. The 8 ml of supernatant, **I** was totally collected and subject to ^{19}F NMR measurement to qunatify free ^{19}F-R8. Then, 4 ml of lysis buffer A (1% Triton X-100, 50 mM Tris, 50 mM EDTA, 150 mM NaCl, 10% D_2O) was added to the pellet, **i**, and left for 15 min on ice to complete the cell membrane solubilization. The solution was centrifuged at 15,000×g for 15 min at 4 °C, to separate the pellet, **ii** and the supernatant, **II**. Then the supernatant, **II** was collected and subjected to ^{19}F NMR measurement (called Lysate). After the measurement, 50 ml of lysis buffer A

was added and centrifuged at 100,000×g for 3 hours at 4 °C. The pellet, **iii** and the supernatant, **III** separated consist of cell membrane and cytosol fractions, respectively.[92] The pellet, **iii** was resuspended in 4 ml of lysis buffer A and subject to the ^{19}F NMR measurement (called Membrane). On the other hand, the supernatant, **III** was lyophilized and resuspended in 4 ml of lysis buffer A, and subject to ^{19}F NMR measurement (called Cytosol). The pellet, **ii** was incubated in 1 ml of lysis buffer A containing 0.5 M NaCl for 15 min on ice, and added to 3 ml of lysis buffer B (0.05% SDS, 0.5% deoxycholic acid, 50 mM Tris-HCl, 5 mM EDTA, 150 mM NaCl, 10% D_2O, pH 7.5). The DNA and cytoskeleton fractions were solubilized and subjected to ^{19}F NMR measurement (called DNA and cytoskeleton). The FIDs were accumulated 10,000-60,000 times to obtain good S/N ratio.

7. REFERENCES

(1) Ringel, M.; Tollman, P.; Hersch, G.; Schulze, U. *Nat. Rev. Drug Discov.* **2013**, *12*, 901–902.

(2) Sawant, R. R.; Patel, N. R.; Torchilin, V. P. *Eur. J. Nanomedicine* **2013**, *5*, 141–158.

(3) Copolovici, D. M.; Langel, K.; Eriste, E.; Langel, Ü. *ACS Nano* **2014**, *8*, 1972–1994.

(4) Lee, S. H.; Castagner, B.; Leroux, J.-C. *Eur. J. Pharm. Biopharm.* **2013**, *85*, 5–11.

(5) Rizzuti, M.; Nizzardo, M.; Zanetta, C.; Ramirez, A.; Corti, S. *Drug Discov. Today* **2014**, *00*, 1–10.

(6) Brock, R. *Bioconjug. Chem.* **2014**, *25*, 863–868.

(7) Patel, L. N.; Zaro, J. L.; Shen, W. **2007**, *24*.

(8) Choi, Y. S.; David, A. E. *Curr. Pharm. Biotechnol.* **2014**, 192–199.

(9) Brasseur, R.; Divita, G. *Biochim. Biophys. Acta* **2010**, *1798*, 2177–2181.

(10) Ziegler, A. *Adv. Drug Deliv. Rev.* **2008**, *60*, 580–597.

(11) Amand, H. L.; Rydberg, H. A.; Fornander, L. H.; Lincoln, P.; Nordén, B.; Esbjörner, E. K. *Biochim. Biophys. Acta* **2012**, *1818*, 2669–2678.

(12) Bechara, C.; Pallerla, M.; Zaltsman, Y.; Burlina, F.; Alves, I. D.; Lequin, O.; Sagan, S.; Pierre, U.; Upmc, C.; Paris, U.; Mixte, U.; Umr, D. R. *FASEB J.* **2013**, *27*, 738–749.

(13) Yang, J.; Tsutsumi, H.; Furuta, T.; Sakurai, M.; Mihara, H. *Org. Biomol. Chem.* **2014**, *12*, 4673–4681.

(14) Tchoumi Neree, A.; Nguyen, P. T.; Chatenet, D.; Fournier, A.; Bourgault, S. *FEBS Lett.* **2014**, 1–7.

(15) Rothbard, J. B.; Kreider, E.; VanDeusen, C. L.; Wright, L.; Wylie, B. L.; Wender, P. a. *J. Med. Chem.* **2002**, *45*, 3612–3618.

(16) Schwieger, C.; Blume, A. *Biomacromolecules* **2009**, *10*, 2152–2161.

(17) Schmidt, N.; Mishra, A.; Lai, G. H.; Wong, G. C. L. *FEBS Lett.* **2010**, *584*, 1806–1813.

(18) Mitchell, D. J.; Kim, D. T.; Steinman, L.; Fathman, C. G.; Rothbard, J. B. *J. Pept. Res.* **2000**, *56*, 318–325.

(19) Amand, H. L.; Fant, K.; Nordén, B.; Esbjörner, E. K.; Åmand, H. L. *Biochem. Biophys. Res. Commun.* **2008**, *371*, 621–625.

(20) Rothbard, J. B.; Jessop, T. C.; Wender, P. a. *Adv. Drug Deliv. Rev.* **2005**, *57*, 495–504.

(21) Herce, H. D.; Garcia, A. E.; Cardoso, M. C. **2014**.

(22) Sakai, N.; Matile, S. *J. Am. Chem. Soc.* **2003**, *125*, 14348–14356.

(23) Rothbard, J. B.; Jessop, T. C.; Lewis, R. S.; Murray, B. a; Wender, P. a. *J. Am. Chem. Soc.* **2004**, *126*, 9506–9507.

(24) Esbjörner, E. K.; Lincoln, P.; Nordén, B. *Biochim. Biophys. Acta* **2007**, *1768*, 1550–1558.

(25) Sakai, N.; Futaki, S.; Matile, S. *Soft Matter* **2006**, *2*, 636–641.

(26) Nishihara, M.; Perret, F.; Takeuchi, T.; Futaki, S.; Lazar, A. N.; Coleman, A. W.; Sakai, N.; Matile, S. *Org. Biomol. Chem.* **2005**, *3*, 1659–1669.

(27) Tsogas, I.; Tsiourvas, D.; Nounesis, G.; Paleos, C. M. *Langmuir* **2005**, *21*, 5997–6001.

(28) Yi, D.; Guoming, L.; Gao, L.; Wei, L. *Biochem. Biophys. Res. Commun.* **2007**, *359*, 1024–1029.

(29) Reuter, M.; Schwieger, C.; Meister, A.; Karlsson, G.; Blume, A. *Biophys. Chem.* **2009**, *144*, 27–37.

(30) Lincoln, P.; Norde, B.; Persson, D.; Thorén, P. E. G.; Esbjörner, E. K.; Goksör, M.; Nordén, B. *Biochim. Biophys. Acta* **2004**, *1665*, 142–155.

(31) Thorén, P. E. G.; Persson, D.; Esbjörner, E. K.; Goksör, M.; Lincoln, P.; Nordén, B. *Biochemistry* **2004**, *43*, 3471–3489.

(32) Tocanne, J.; Teissié, J. *Biochim. Biophys. Acta - Rev. Biomembr.* **2015**, *4157*, 10–12.

(33) Zannoni, C.; Arcioni, A.; Cavatorta, P. *Chem. Phys. Lipids* **1983**, *32*, 179–250.

(34) Fiorini, R.; Valentino, M.; Wang, S.; Glaser, M.; Gratton, E. *Biochemistry* **1987**, *26*, 3864–3870.

(35) Kaiser, R.; London, E. *Biochemistry* **1998**, *2960*, 8180–8190.

(36) Lakowicz, J. R.; Masters, B. R. *Principles of Fluorescence Spectroscopy*; Third Edit.; Springer: New York, 2006.

(37) Asuncion-Punzalan, E.; Kachel, K.; London, E. *Biochemistry* **1998**, *37*, 4603–4611.

(38) Stryer, L. *J. Am. Chem. Soc.* **1966**, *88*, 5708–5712.

(39) Stubbs, C. D.; Ho, C.; Slater, S. J. *J. Fluoresc.* **1995**, *5*, 19–28.

(40) Ho, C.; Slater, S. J. S.; Stubbs, C. D. C. *Biochemistry* **1995**, *34*, 6188–6195.

(41) Seelig, J. *Biochim. Biophys. Acta (BBA)-Reviews Biomembr.* **1997**, *1331*, 103–116.

(42) Maximilian, C. *Proteins* **1996**, *24*, 1–2.

(43) White, S. H.; Wimley, W. C. *Annu. Rev. Biophys. Biomol. Struct.* **1999**, *28*, 319–365.

(44) White, S. H.; Wimley, W. C. *Biochim. Biophys. Acta* **1998**, *1376*, 339–352.

(45) Herce, H. D.; Garcia, A. E. *Proc. Natl. Acad. Sci. U. S. A.* **2007**, *104*, 20805–20810.

(46) Herce, H.; Garcia, A. *J. Biol. Phys.* **2007**, *33*, 345–356.

(47) Palm-Apergi, C.; Lorents, A.; Padari, K.; Pooga, M.; Hällbrink, M. *FASEB J.* **2009**, *23*, 214–223.

(48) Konate, K.; Crombez, L.; Deshayes, S.; Decaffmeyer, M.; Thomas, A.; Brasseur, R.; Akashi, K.; Heitz, F.; Divita, G. *Biochemistry* **2010**, *49*, 3393–3402.

(49) Schmidt, N. W.; Mishra, A.; Lai, G. H.; Davis, M.; Sanders, L. K.; Tran, D.; Garcia, A.; Tai, K. P.; McCray, P. B.; Ouellette, A. J.; Selsted, M. E.; Wong, G. C. L. *J. Am. Chem. Soc.* **2011**, *133*, 6720–6727.

(50) Mishra, A.; Hwee, G.; Schmidt, N. W.; Sun, V. Z.; Rodriguez, A. R.; Tong, R.; Tang, L.; Lai, G. H.; Cheng, J.; Deming, T. J.; Kamei, D. T.; Wong, G. C. L. *Proc. Natl. Acad. Sci. U. S. A.* **2011**, *108*, 16883–16888.

(51) Hirose, H.; Takeuchi, T.; Osakada, H.; Pujals, S.; Katayama, S.; Nakase, I.; Kobayashi, S.; Haraguchi, T.; Futaki, S. *Mol. Ther.* **2012**, *20*, 984–993.

(52) Seelig, J. *Biochim. Biophys. Acta* **2004**, *1666*, 40–50.

(53) Gonçalves, E.; Kitas, E.; Seelig, J.; Goncalves, E. *Biochemistry* **2005**, *44*, 2692–2702.

(54) Hitz, T.; Iten, R.; Gardiner, J.; Namoto, K.; Walde, P.; Seebach, D. *Biochemistry* **2006**, *45*, 5817–5829.

(55) Jasanoff, A.; Fersht, A. R. *Biochemistry* **1994**, *33*, 2129–2135.

(56) Roccatano, D.; Colombo, G.; Fioroni, M.; Mark, A. E. **2002**, *99*, 2–7.

(57) El-Sayed, A.; Khalil, I. a; Kogure, K.; Futaki, S.; Harashima, H. *J. Biol. Chem.* **2008**, *283*, 23450–23461.

(58) Bechara, C. C.; Sagan, S. *FEBS Lett.* **2013**, *587*, 1693–1702.

(59) Meerovich, I.; Muthukrishnan, N.; Johnson, G. a; Erazo-Oliveras, A.; Pellois, J.-P. *Biochim. Biophys. Acta* **2014**, *1840*, 507–515.

(60) Dupont, E.; Prochiantz, A.; Joliot, A. *J. Biol. Chem.* **2007**, *282*, 8994–9000.

(61) Szeto, H. H.; Schiller, P. W.; Zhao, K.; Luo, G. *FASEB J.* **2005**, *19*, 118–120.

(62) Puckett, C. a; Barton, J. K. *J. Am. Chem. Soc.* **2009**, *131*, 8738–8739.

(63) Bertrand, J.-R.; Malvy, C.; Auguste, T.; Tóth, G. K.; Kiss-Ivánkovits, O.; Illyés, E.; Hollósi, M.; Bottka, S.; Laczkó, I. *Bioconjug. Chem.* **2009**, *20*, 1307–1314.

(64) Aubry, S.; Aussedat, B.; Delaroche, D.; Jiao, C.-Y.; Bolbach, G.; Lavielle, S.; Chassaing, G.; Sagan, S.; Burlina, F. *Biochim. Biophys. Acta* **2010**, *1798*, 2182–2189.

(65) Lécorché, P.; Walrant, A.; Burlina, F.; Dutot, L.; Sagan, S.; Mallet, J.; Desbat, B.; Chassaing, G.; Alves, I. D.; Lavielle, S. *Biochim. Biophys. Acta* **2012**, *1818*, 448–457.

(66) Walrant, A.; Matheron, L.; Cribier, S.; Chaignepain, S.; Jobin, M.-L.; Sagan, S.; Alves, I. D. *Anal. Biochem.* **2013**, *438*, 1–10.

(67) Serber, B. Z.; Corsini, L.; Durst, F.; Serber, Z.; Dötsch, V. *Methods Enzymol.* **2005**, *394*, 17–41.

(68) Suzuki, Y.; Brender, J. J. R.; Hartman, K.; Ramamoorthy, A.; Marsh, E. N. G. *Biochemistry* **2012**, *51*, 8154–8162.

(69) Shi, P.; Li, D.; Chen, H.; Xiong, Y.; Wang, Y.; Tian, C. *Protein Sci.* **2012**, *21*, 596–600.

(70) Kitevski-Leblanc, J. L.; Hoang, J.; Thach, W.; Larda, S. T.; Prosser, R. S. *Biochemistry* **2013**, *52*, 5780–5789.

(71) Vega, M. De; Marin, M.; Kondo, N.; Miyauchi, K.; Kim, Y.; Epand, R. F. R. M.; Melikyan, G. B.; de la Vega, M. *Retrovirology* **2011**, *8*, 99.

(72) Capila, I.; Linhardt, R. J. *Angew. Chemie* **2002**, *41*, 391–412.

(73) Ziegler, A.; Seelig, J.; Ziegler, A. *Biophys. J.* **2004**, *86*, 254–263.

(74) Futamura, M.; Dhanasekaran, P.; Handa, T.; Phillips, M. C.; Lund-Katz, S.; Saito, H. *J. Biol. Chem.* **2005**, *280*, 5414–5422.

(75) Blaum, B. S.; Deakin, J. a; Johansson, C. M.; Herbert, A. P.; Barlow, P. N.; Lyon, M.; Uhrín, D. *J. Am. Chem. Soc.* **2010**, *132*, 6374–6381.

(76) Noborn, F.; Callaghan, P. O.; Hermansson, E.; Zhang, X.; Ancsin, J. B.; Damas, A. M.; Dacklin, I.; O'Callaghan, P.; Presto, J.; Johansson, J.; Saraiva, M. J.; Lundgren, E.; Kisilevsky, R.; Westermark, P.; Li, J.-P. *Proc. Natl. Acad. Sci. U. S. A.* **2011**, *108*, 5584–5589.

(77) Solomon, J. P.; Bourgault, S.; Powers, E. T.; Kelly, J. W. *Biochemistry* **2011**, *50*, 2486–2498.

(78) Emiko Okamura, Keiko Ninomiya, Shiroh Futaki, Yasuharu Nagai, Tomohiro Kimura, Chihiro Wakai, Nobuyuki Matubayasi, Yukio Sugiura, M. N. *Chem. Lett.* **2005**, *34*, 1064–1065.

(79) Okamura, E.; Yoshii, N. *J. Chem. Phys.* **2008**, *129*, 215102.

(80) Lopes, S.; Simeonova, M.; Gameiro, P.; Rangel, M.; Ivanova, G. *J. Phys. Chem. B* **2012**, *116*, 667–675.

(81) Takechi, Y.; Saito, H.; Okamura, E. *Chem. Phys. Lett.* **2013**, *570*, 136–140.

(82) Henriques, S.; Melo, M.; Castanho, M. *Biochem. J.* **2006**, *7*, 1–7.

(83) Clark, K. S.; Svetlovics, J.; McKeown, A. N.; Huskins, L.; Almeida, P. F. *Biochemistry* **2011**, *50*, 7919–7932.

(84) Last, N. B.; Schlamadinger, D. E.; Miranker, A. D. *Protein Sci.* **2013**, *22*, 1–13.

(85) El-andaloussi, S.; Arver, P. J.; Johansson, H. J.; Järver, P.; Langel, U. *Biochem. J.* **2007**, *407*, 285–292.

(86) Jo, J.; Hong, S.; Choi, W. Y.; Lee, D. R. *Sci. Rep.* **2014**, *4*, 4378.

(87) Tanaka, M.; Tanaka, T.; Ohta, S.; Kawakami, T.; Konno, H.; Akaji, K.; Aimoto, S.; Saito, H. *J. Pept. Sci.* **2009**, *15*, 36–42.

(88) Aki, K.; Fujii, N. N. *PLoS One* **2013**, *8*, e58515.

(89) Tamba, Y.; Terashima, H.; Yamazaki, M. *Chem. Phys. Lipids* **2011**, *164*, 351–358.

(90) Bartlett, G. R. *J. Biol. Chem.* **1959**, *234*, 466–468.

(91) Scholtz, J. M.; Qian, H.; York, E. J.; Stewart, J. M.; Baldwin, R. L. *Biopolymers* **1991**, *31*, 1463–1470.

(92) Tohyama, Y.; Yanagi, S.; Sada, K.; Yamamura, H. *J. Biol. Chem.* **1994**, *269*, 32796–32799.

8. ACKNOWLEDGEMENTS

I would like to express my sincere gratitude to my supervisor, Professor Hiroyuki Saito in The University of Tokushima for giving me this precious study opportunity. His elaborated guidance, considerable encouragement, and invaluable discussion made my research of great achievement and my study life unforgettable.

I am very grateful to Associate Professor Keiichiro Okuhira and Assistant Professor Kazuchika Nishitsuji in the University of Tokushima, Administrative Director and Associate chancellor Saburo Aimoto, Professor Hironobu Hojo, and Associate Professor Toru Kawakami in Osaka University, Professor Emiko Okamura and Professor Yumi Tohyama in Himeji Dokkyo University, and University Lecturer Masafumi Tanaka in Kobe pharmaceutical University for their valuable cooperation in my study.

I am also very grateful to my colleagues in the laboratory of molecular physical pharmaceutics at the University of Tokushima for their helpful discussions.

Finally, I would like to extend my appreciation to my family for their understanding, support, and encouragement throughout my study. My heartfelt appreciation goes to my wife.